

# High-Order Flux Reconstruction Schemes with Minimal Dispersion and Dissipation

Kartikey Asthana · Antony Jameson

Received: 19 February 2014 / Revised: 14 June 2014 / Accepted: 18 June 2014  
© Springer Science+Business Media New York 2014

**Abstract** Modal analysis of the flux reconstruction (FR) formulation is performed to obtain the semi-discrete and fully-discrete dispersion relations, using which, the wave properties of physical as well as spurious modes are characterized. The effect of polynomial order, correction function and solution points on the dispersion, dissipation and relative energies of the modes are investigated. Using this framework, a new set of linearly stable high-order FR schemes is proposed that minimizes wave propagation errors for the range of resolvable wavenumbers. These schemes provide considerably reduced error for advection in comparison to the Discontinuous Galerkin scheme and benefit from having an explicit differential update. The corresponding resolving efficiencies compare favorably to those of standard high-order compact finite difference schemes. These theoretical expectations are verified by a comparison of proposed and existing FR schemes in advecting a scalar quantity on uniform as well as non-uniform grids.

**Keywords** High-order · Flux reconstruction · Discontinuous Galerkin · dispersion · Dissipation · Wave propagation

**Mathematics Subject Classification** 65M60 · 35P05 · 39A14

## 1 Introduction

In the last two decades, high-order methods have emerged as a feasible option for high accuracy solutions in fluid mechanics, particularly in aeroacoustics [1–3] and, to limited extent, in turbulence [4]. The error in the numerical solution for a formally  $N$ th order method is asymptotically bounded above by a term of order  $h^{N+1}$  where  $h$  is the grid spacing. The exponential dependence on  $N$  enables high-order methods to provide higher accuracy for the same number of degrees of freedom [5] as compared to conventional 2nd order methods.

---

K. Asthana (✉) · A. Jameson  
Department of Aeronautics and Astronautics, Stanford University, Stanford, CA 94305, USA  
e-mail: kasthana@stanford.edu

Owing to their ease of implementation, compact finite difference schemes [6] have been employed widely for high-order computing, and extensions to curvilinear and deforming meshes have also been proposed [7]. However, the application of finite difference schemes to modern industrial problems remains limited due to the difficulty involved in generating structured meshes for complex geometries. A popular instance of high-order methods that can treat general unstructured meshes while retaining a compact mass matrix is the Discontinuous Galerkin (DG) method [8–10]. The method has been extensively analyzed and applied to several conservation laws including the Navier–Stokes equations. Recently, Huynh [11] proposed a flux reconstruction (FR) approach that provides a differential framework for discontinuous finite element schemes. Besides the advantage of an identity mass matrix, the FR framework, at least for linear fluxes, recovers the collocation based nodal DG method as well as the Spectral Difference (SD) method [12, 13]. The general framework allows for the definition of new schemes as well, which has led to the development of energy stable FR schemes for linear [14] as well as non-linear fluxes [15]. The approach has been extended to triangular [16, 17] and tetrahedral elements [18] and to general advection-diffusion problems [19].

For problems involving propagation of disturbances in physical variables, a relevant measure of accuracy can be based on the the fraction of resolvable wavenumbers for which constituent waves would be propagated with negligible numerical dispersion and dissipation. Such problems appear naturally in aeroacoustics and time dependent viscous flows involved in transition studies. The non-conservative form of a hyperbolic system of equations provides a functional dependence of the wavespeeds on wavenumber which is denoted as the analytical dispersion relation [20]. Similarly, the discrete numerical system corresponding to a particular numerical scheme provides a numerical dispersion relation. Spectral analysis of the numerical dispersion relation was first utilized by Tam et al. [21] to obtain dispersion relation preserving finite difference schemes for aeroacoustics, which facilitated the development and optimization of several implicit compact difference schemes [6, 22–25] with near-spectral resolution. Although schemes with high formal accuracy generally provide higher spectral resolution than their low-order counterparts, this is not always true as was shown by Lele [6] who showed that an optimized 4th order scheme can provide higher spectral resolution than a 10th order explicit central difference scheme. With the exception of spectral methods [26], most numerical methods preserve the dispersion relation only for low wavenumbers, and introduce significant dispersion and/or dissipation beyond a critical wavenumber denoted as the resolving efficiency. However, spectral methods are not easily applicable to complex flow geometries where the DG method and finite volume schemes have obtained great success. An analysis of the DG method for wave propagation problems was carried out by Hu et al. [27]. It was shown that the  $P$ th order DG method applied to linear advection results in one physical mode and  $P$  spurious or parasitic modes which get damped out quickly on account of relatively high dissipation. In [28], the wave-properties for DG in the case of non-uniform grids were investigated by specifying temporal frequencies and studying the numerical spatial waves. It was shown that the dispersion error for the physical mode is of order  $2P + 3$  and the dissipation error is of order  $2P + 2$ . The variation of dispersion and dissipation errors with polynomial order  $P$  was further rigorously established by Ainsworth [29] who proved that for a fixed mesh of spacing  $h$ , these errors decay at an exponential rate when  $2P + 1 \approx \kappa kh$ , where  $k$  is the wavenumber and  $\kappa > 1$  is some constant.

Focusing on FR schemes, the first insight into spectral properties was provided by Huynh himself [11], wherein Fourier analysis applied to 1-D advection, with fully upwinded Riemann flux at the interface, was utilized to recognize the presence of principal and spurious

eigenvalues. Taylor expansion of the principal eigenvalue was used to define an order of accuracy in the spectral space and it was proven that this order is independent of the choice of solution points. Additionally, the variation of the principal eigenvalue over the range of resolvable wavenumbers was used to ascertain numerical stability limits for several FR schemes. Another study was conducted by Vincent et al. [30] where Fourier analysis was employed to study the wave properties of energy stable schemes known as ESFR or VCJH [14, 15] schemes. In that investigation, the authors employed an automated procedure based on modal analysis to combine all the numerical modes into a single functional relationship between the wavespeed and the wavenumber. It was suggested that this functional relationship is representative of the dispersive and dissipative properties of the scheme and that multiple modes should not be identified distinctly. A highlight of the study was the identification of the ‘ $c_+$ ’ scheme that offers the highest CFL limit obtained when the ESFR parameter  $c$  is chosen to be equal to  $c_+$  for a given polynomial order.

In this paper, we first perform a direct modal analysis of the FR formulation to obtain the semi-discrete dispersion relation which provides dispersion and dissipation properties for all the  $P + 1$  numerical modes, where  $P$  is the polynomial order. Modal decomposition of the initial condition is carried out to ascertain that the spurious modes contain non-zero energy especially at high wavenumbers. It is shown that in addition to polynomial order and choice of correction function, the choice of solution points is also important even for linear fluxes. The second part of the paper deals with an optimization problem to provide correction functions that minimize wave propagation errors for a given polynomial order. The resolving efficiency of these optimal schemes offer significant improvement over the DG scheme and compare well with conventional compact finite difference schemes.

The paper is formatted as follows. In Sect. 2, the FR formulation is applied to 1-D advection and modal analysis is performed to determine dispersion, dissipation and energy fractions corresponding to the numerical modes. In Sect. 3, the relevant minimization problem is defined and optimal FR schemes are computationally derived that minimize wave propagation errors. In Sect. 4, the limiting CFL values for these schemes are compared with those for existing FR schemes. Finally, in Sect. 5, advection of a wave packet on uniform and non-uniform grids is considered as a test case to verify the analytical expectations.

## 2 Fourier Analysis of FR Schemes: Energy Distribution Between the Physical Mode and Spurious Modes

We begin with a very brief description of the FR formulation to arrive at the update equation for 1-D advection which forms the governing system for all subsequent analysis. Bloch waves are introduced into the update to obtain the semi-discrete dispersion relation, which in turn provides dispersion and dissipation for each of the numerical modes. These results are then utilized to study the effect of polynomial order, correction function and solution points on the dispersion properties. The discrete initial condition is modally expanded in the eigenvector basis to obtain the initial distribution of energy among the numerical modes as a function of wavenumber. This distribution is important as it determines the relative weights of numerical modes in the overall numerical solution. Since the spurious numerical modes are highly dispersive and quite dissipative at low to moderate wavenumbers, the loss in accuracy of the numerical solution is directly related to the fraction of energy captured by these modes. Moreover, for high wavenumbers, the numerical dissipation associated with the spurious modes can be lower than that for the physical mode, so that after enough time, the high wavenumber components of the numerical solution become totally spurious.

### 2.1 FR Formulation for 1-D Advection

A detailed account of the FR framework can be found in [11,30]. Consider a 1-D scalar conservation law

$$\begin{aligned} \frac{\partial u}{\partial t} + \frac{\partial f(u)}{\partial x} &= 0 \quad \text{in } \Omega \in \mathbb{R}, \quad t > 0 \\ u(x, 0) &= u_0(x) \end{aligned} \tag{1}$$

where the flux  $f(u)$  is possibly non-linear. The domain  $\Omega$  is partitioned into  $n_{el}$  elements  $\Omega = \bigcup_{j=1}^{n_{el}} \Omega_j$  of variable width  $h_j = x_{j+1} - x_j$ . Each element is discretized into  $P + 1$  solution points  $\{x_{j,1}, x_{j,2}, \dots, x_{j,P+1}\}$  distributed variably. The discontinuous solution and flux are both defined as interpolating polynomials in the  $j$ th element

$$u_j^\delta(x) = \sum_{p=1}^{P+1} u_{j,p}^\delta l_{j,p}(x) \tag{2}$$

$$f_j^\delta(x) = \sum_{p=1}^{P+1} f(u_{j,p}^\delta) l_{j,p}(x) \tag{3}$$

where  $l_{j,p}$  is the  $p$ th Lagrange polynomial in the  $j$ th element, and the superscript  $\delta$  denotes a numerically evaluated quantity. Conservation is explicitly incorporated into the formulation by first defining common interface fluxes between elements

$$\begin{aligned} f^{int}(x_j) &= f^{int}(u_{j-1}^\delta(x_j), u_j^\delta(x_j)) \\ f^{int}(x_{j+1}) &= f^{int}(u_j^\delta(x_{j+1}), u_{j+1}^\delta(x_{j+1})) \end{aligned} \tag{4}$$

and then correcting the discontinuous flux through correction functions. These correction functions,  $g_L(x)$  and  $g_R(x)$ , are of order  $P + 1$ , being binary on the boundaries (the left correction function  $g_L(x)$  is 1 on the left boundary, 0 on the other and vice-versa) and approximate zero internally. The corrected flux, denoted by superscript  $(\delta, c)$ , then becomes

$$f_j^{\delta,c}(x) = f_j^\delta(x) + (f^{int}(x_j) - f_j^\delta(x_j))g_L(x) + (f^{int}(x_{j+1}) - f_j^\delta(x_{j+1}))g_R(x) \tag{5}$$

and takes the common interface values at the edges but is not necessarily equal to the discontinuous flux values internally. For convenience, an isoparametric mapping is introduced from the physical domain  $x \in \Omega_j = [x_j, x_{j+1}]$  to the parent domain  $\xi \in [-1, 1]$  as

$$\xi|_{\Omega_j}(x) = 2 \frac{x - x_j}{x_{j+1} - x_j} - 1 \tag{6}$$

such that the  $p$ th Lagrange function  $l_{j,p}(x)$  transforms as  $l_{j,p}(\xi)$  and the solution points become  $\{\xi_{j,1}, \xi_{j,2}, \dots, \xi_{j,P+1}\}$ . The discrete numerical solution can now be updated using the derivative of the corrected flux at the solution points. Owing to the differential construction, the update step does not involve a mass matrix. Denoting  $\mathbf{u}_j^\delta$  as the discrete solution in the  $j$ th element and  $\mathbf{f}_j^\delta$  as the discrete flux, the update can be expressed as

$$\frac{d^\delta}{dt} \mathbf{u}_j^\delta = -J_j^{-1} \left[ \mathbf{D}_j \mathbf{f}_j^\delta + (f^{int}(x_j) - f_j^\delta(x_j)) \mathbf{g}_{L,\xi} + (f^{int}(x_{j+1}) - f_j^\delta(x_{j+1})) \mathbf{g}_{R,\xi} \right] \tag{7}$$

where  $J_j = h_j/2$  is the Jacobian,  $\mathbf{D}_j$  is the discrete derivative operator such that  $D_{j,p,m} = \frac{dl_{j,m}}{d\xi}(\xi_{j,p})$ , and  $\mathbf{g}_{L,\xi}, \mathbf{g}_{R,\xi}$  are the derivatives of the correction functions at the solution points.

The  $\frac{d^\delta}{dt}$  operator denotes that the time derivative is not exact but is approximated numerically during the update.

The control parameters in the FR formulation are (i) choice of solution points  $\xi_p$  for  $p = 1, 2, \dots, P + 1$ , (ii) choice of the interface flux  $f^{int}$ , and most importantly (iii) choice of correction functions  $g_L(x)$  and  $g_R(x)$ . With Gauss–Legendre points as solution points, selecting the left boundary correction as the right Radau polynomial, and vice versa, recovers the DG scheme at least for linear fluxes. Similarly, selecting the correction functions to have zeros at the flux collocation points recovers a version of the SD scheme, again, at least for linear fluxes.

The 1-D FR formulation above can be applied to advection by considering the linear flux  $f(u) = au$ , so that the conservation equation, in some  $(x', t')$  coordinates, becomes  $\frac{\partial u}{\partial t'} + a \frac{\partial u}{\partial x'} = 0$ . For the sake of simplicity, assume that the grid is uniform,  $h_j = h$  for  $j = 1, 2, \dots, n_{el}$ , and that the distribution of solution points is identical among elements. Non-dimensionalize the equation using the length scale as the element width  $x = x'/h$ , and the velocity scale as the advection speed  $t = t'a/h$ , so that the conservation equation becomes

$$\frac{\partial u}{\partial t} + \frac{\partial u}{\partial x} = 0 \tag{8}$$

Since the direction of information propagation is explicitly known for advection, the flux can be fully upwinded so that  $f^{int}(x_j) = u_{j-1}^\delta(x_j)$ . The numerical update can then be rewritten with explicit coupling between the elements

$$\frac{d^\delta}{dt} \mathbf{u}_j^\delta = -J_j^{-1} \left[ \mathbf{C}_0 \mathbf{u}_j^\delta + \mathbf{C}_{-1} \mathbf{u}_{j-1}^\delta \right] \tag{9}$$

where

$$\begin{aligned} \mathbf{C}_0 &= \mathbf{D} - \mathbf{g}_{L,\xi} \mathbf{l}_L^T \\ \mathbf{C}_{-1} &= \mathbf{g}_{L,\xi} \mathbf{l}_R^T \end{aligned} \tag{10}$$

and  $\mathbf{l}_L$  and  $\mathbf{l}_R$  are the vectors containing the values of the Lagrange polynomials at the left and right interfaces respectively.

### 2.2 Bloch Waves and Semi-discrete Dispersion Relation

For a monochrome initial condition,  $e^{ikx}$  of wavelength  $2\pi/k$ , Eq. (8) admits an analytical solution of the form

$$u(x, t) = e^{ik(x-t)} \tag{11}$$

which are essentially Bloch waves of wavenumber  $k$  and can be expressed conveniently in the parent domain as

$$u(x \in \Omega_j, t) = e^{ik(j-t)} e^{ik \frac{(\xi+1)}{2}} \tag{12}$$

using the isoparametric map in Eq. (6) and noting that  $h = 1$  due to the choice of non-dimensionalization. Modal analysis of finite difference schemes [6,21,25] employ this explicit form directly into the numerical update step. However, by construction, the discontinuous solution in the FR framework is restricted to the function space spanned by the Lagrangian polynomial basis. Since the exponential Bloch wave is infinitely dimensional in polynomial space, it must be projected [27,29,30] to obtain a relevant general form of the numerical solution. The discrete solution can then be expressed as

$$\mathbf{u}_j^\delta(t) = e^{ik(j-a^\delta(k)t)} \mathbf{v} \tag{13}$$

where  $a^\delta(k) \in \mathbb{C}$  is the wavespeed with which the numerical solution advects, and  $\mathbf{v}$  is the unknown vector associated with the projection (discussed further in Sect. 2.5). Admission of this general numerical solution into the FR vectorial update step Eq. (9), with an exact time derivative operator, provides the semi-discrete dispersion relation

$$\mathbf{M}\mathbf{v} = a^\delta \mathbf{v} \tag{14}$$

where  $\mathbf{M} = \frac{-2i}{k} (\mathbf{C}_0 + e^{-ik} \mathbf{C}_{-1})$ .

Owing to the multiplicity in the degrees of freedom available within each element, the numerical dispersion relation manifests as a  $P + 1$  dimensional eigenvalue problem for each wavenumber  $k$ . As is typical of finite element schemes, one obtains  $P + 1$  numerical modes where the corresponding eigenvalues  $a_p^\delta(k) = a_{p_r}^\delta(k) + ia_{p_i}^\delta(k)$  for  $p = 1, 2, \dots, P + 1$  relate directly to the numerical wavespeeds. The analytical solution Eq. (11) provides the exact dispersion relation as  $a_r = 1, a_i = 0$  which implies that all wavenumbers must advect at the advection velocity without change in amplitude. Expanding the numerical solution as

$$\mathbf{u}_j^\delta(t) = e^{ka_{p_i}^\delta t} e^{ik(j-a_{p_r}^\delta t)} \mathbf{v} \tag{15}$$

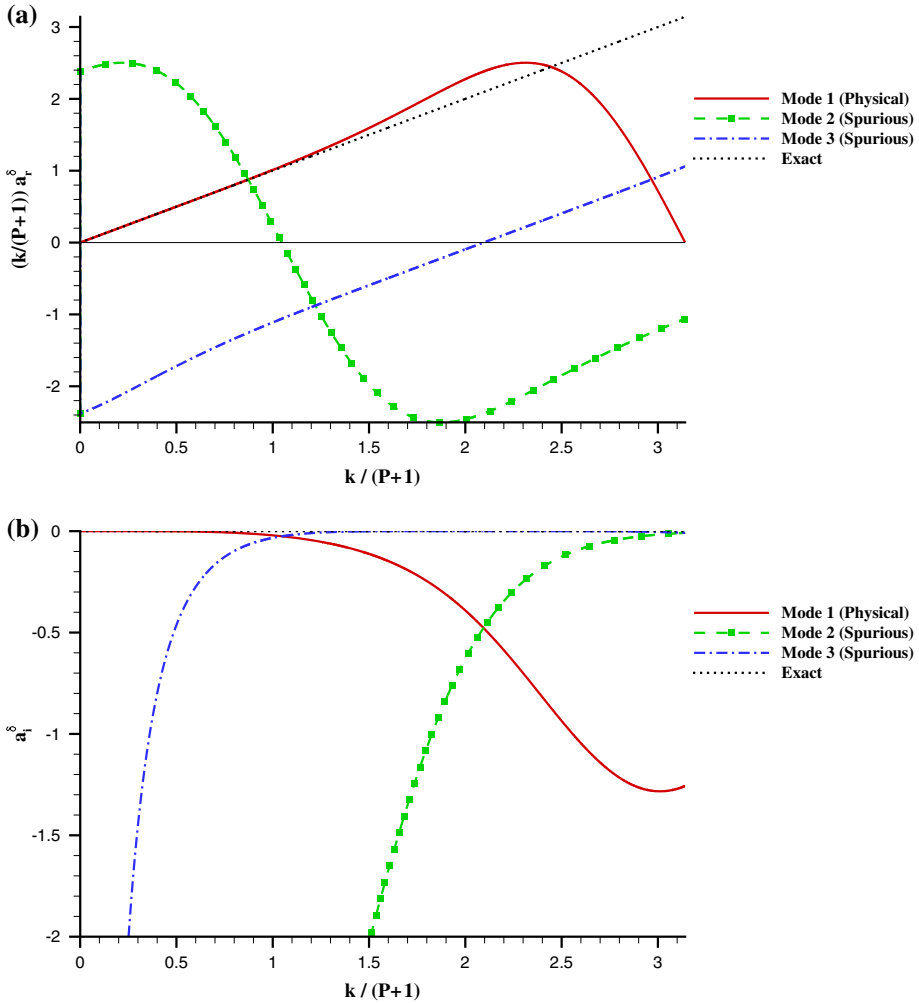
allows one to define dispersive and dissipative errors as  $e^{ik(1-a_{p_r}^\delta t)}$  and  $e^{ka_{p_i}^\delta t}$  respectively, which can be obtained from the solution of the eigenvalue problem, Eq. (14).

Figure 1a, b plot the real and imaginary parts of the numerical wavespeeds corresponding to all the numerical modes for the DG scheme recovered via FR for  $P = 2$  on Gauss–Legendre solution points. The real part of the numerical wavespeed is plotted in the form of an effective wavenumber  $k_{eff} = k a_r^\delta / (P + 1)$  while the imaginary part is plotted directly. The wavenumber is normalized by the number of intra-element degrees of freedom to have the Nyquist limit as  $\pi$ . For reference, the analytical wavespeed components are also included. These modes are in good agreement with the results of Hu et al. [27] where the analysis was performed starting directly from the DG framework. As noted in [27], only one of the  $P + 1$  numerical modes follows the analytical expectation and is hereafter referred to as the physical mode. This mode preserves the dispersion relation till about a third of the resolved spectrum. For higher wavenumbers, upwinding in the scheme adds numerical dissipation (Fig. 1b) while numerical dispersion (Fig. 1a) causes the corresponding Bloch waves to move faster than the advection velocity until a crossover point whereafter they slow down to zero at the Nyquist limit.

The other  $P$  modes are spurious and are characterized by excessive dispersion errors ( $e^{ik(1-a_{p_r}^\delta t)}$ ) as can be seen from Fig. 1a. Corresponding plots for  $P = 5$  are provided in Fig. 2a, b. For a given polynomial order, half of the spurious modes (even numbered modes for odd  $P$  and vice versa) are least dissipative at high wavenumbers and have a smaller, possibly negative, real part of the wavespeed. Fortunately, these modes are the least energetic as well (Sect. 2.5). The other half of the spurious modes are more dissipative, particularly at high wavenumbers, and are characterized by a crossover point where they cross the analytical expectation. These modes can have a considerable fraction of the energy at high wavenumbers.

### 2.3 Effect of Polynomial Order

Figure 3a, b plot the real and imaginary part of the numerical wavespeed corresponding to the physical mode for the DG scheme recovered via FR for  $P = 1$  to 5 against the normalized wavenumber. The range of resolvable wavenumbers, defined by the Nyquist limit, increases in proportion to the number of degrees of freedom within each element. Interestingly, even the range of normalized wavenumbers  $k/(P + 1)$  over which are the dispersion relation is



**Fig. 1** **a** Effective wavenumber  $k_{eff} = k a_i^\delta / (P + 1)$  and **b** imaginary part  $a_i^\delta$  of the numerical wavespeed for the 3 numerical modes for DG scheme via FR for  $P = 2$

approximately preserved, increases with polynomial order. While higher polynomial order results in greater overshoot (Fig. 3a) suggesting a lower CFL limit, the dominant effect is that of reduced dissipation (3b), leading to an increase in resolving efficiency. These results are again in agreement with those of Hu et al. [27] for the DG scheme, and with Ainsworth [29] who shows that the leading coefficient of dispersion and dissipation errors decreases rapidly with increasing polynomial order.

### 2.4 Effect of Correction Function

Figure 4a, b plot the real and imaginary part of the numerical wavespeed corresponding to the physical mode for the DG, SD and Huynh’s  $g_2$  [14] scheme recovered via FR for  $P = 3$  against the normalized wavenumber. The choice of correction function has a critical impact on both the real and imaginary parts of the numerical wavespeed for the physical

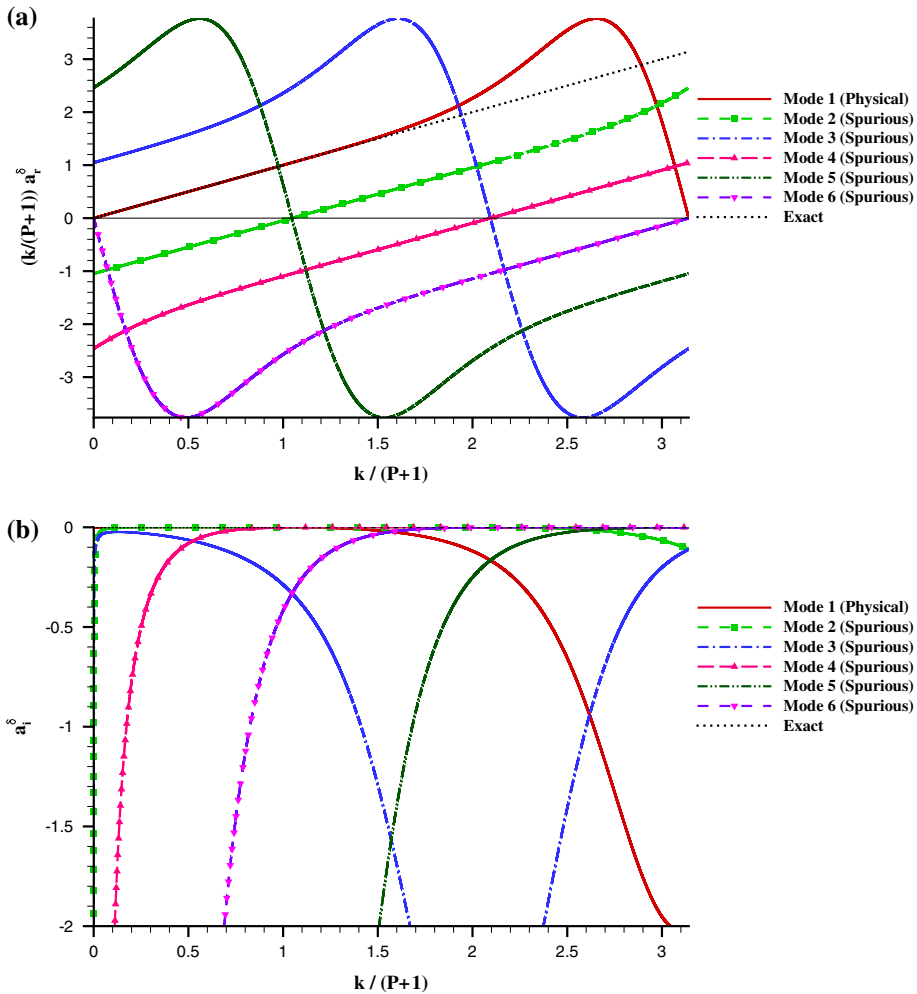


**Fig. 2** **a** Effective wavenumber  $k_{eff} = k a_r^\delta / (P + 1)$  and **b** imaginary part  $a_i^\delta$  of the numerical wavespeed for the 6 numerical modes for DG scheme via FR for  $P = 5$

mode. For these three schemes, a competing effect can be observed between the dispersion and dissipation errors. In comparison to DG, for the SD scheme, while the real part of the wavespeed stays nearly accurate for a larger range of wavenumbers, the imaginary part starts deviating earlier, suggesting the possibility of an optimal choice somewhere in between. These results are identical to the observations of Vincent et al. [30] wherein the authors used an automated modal energy based sampling procedure, following Van den Abeele [31], to recover a single Fourier mode for any polynomial order. This suggests that the modal reconstruction procedure employed therein, in fact recovered the physical mode.

### 2.5 Effect of Solution Points and Relative Modal Energies

Conventionally, the spurious modes are often disregarded as they are usually quite dissipative, for low to moderate wavenumbers, and do not significantly contaminate the physical mode.



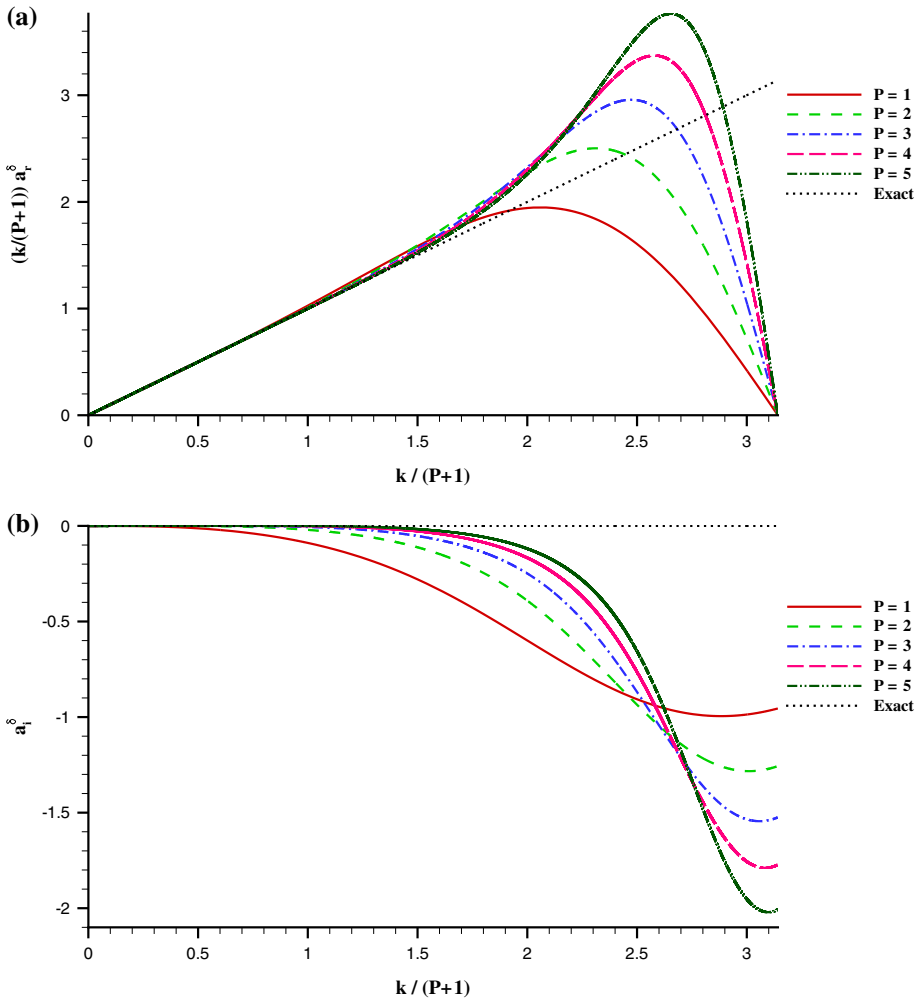


**Fig. 3** Effect of polynomial order: **a** effective wavenumber  $k_{eff} = k a_r^\delta / (P + 1)$  and **b** imaginary part  $a_i^\delta$  of the numerical wavenumber for the physical mode for DG scheme via FR for  $P = 1$  to 5

However, the fraction of energy contained within the spurious modes is lost. Moreover, from Fig. 1b and 2b, one notes that, for FR schemes, spurious modes can possibly have very low dissipation at high wavenumbers. Hence, after a long enough time, the solution at high wavenumbers may get constituted entirely from spurious modes once the physical mode has decayed.

The distribution of energy among the  $P + 1$  modes is determined by the projection of the initial condition onto the polynomial basis. Owing to the Lagrangian nature of the basis, the numerical initial condition is exact at the solution points which define the interpolant in Eq. (2). This can be expressed using Eqs. (12) and (13) as

$$\begin{aligned}
 u(x_{j,p}, 0) &= u^\delta(x_{j,p}, 0) \\
 e^{ikj} e^{ik \frac{(x_{j,p}-x_j)}{2}} &= e^{ikj} v_p \quad \text{for } p = 1, 2, \dots, P + 1
 \end{aligned}
 \tag{16}$$

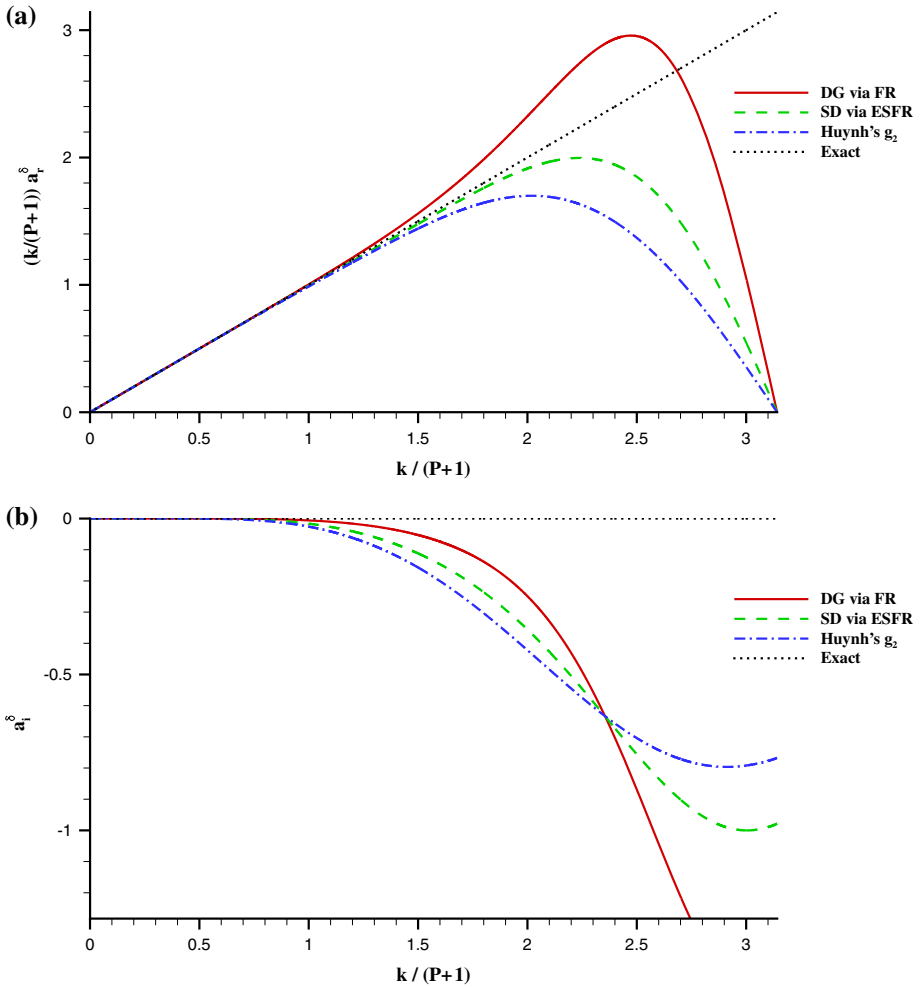


**Fig. 4** Effect of correction function: **a** Effective wavenumber  $k_{eff} = k a_r^\delta / (P + 1)$  and **b** imaginary part  $a_i^\delta$  of the numerical wavenumber for the physical mode for DG, SD and Huynh's  $g_2$  scheme (via FR) for  $P = 3$

which yields

$$v_p = e^{ik \frac{(\xi_{p+1})}{2}} \tag{17}$$

The discrete numerical initial condition can now be expressed vectorially in modal coordinates

$$e^{ik \frac{(\xi+1)}{2}} = \sum_{p=1}^{P+1} \lambda_p \mathbf{v}_p^\delta = \mathbf{V} \Lambda \tag{18}$$

where the modal coefficients  $\lambda_p$  are the respective weights of the  $P + 1$  eigenvectors, and  $\xi = [\xi_1, \xi_2, \dots, \xi_{P+1}]^T$  is the vector of solution points. Since the energy of a traveling wave is proportional to square of the amplitude, a measure of the relative energy among modes can be defined as

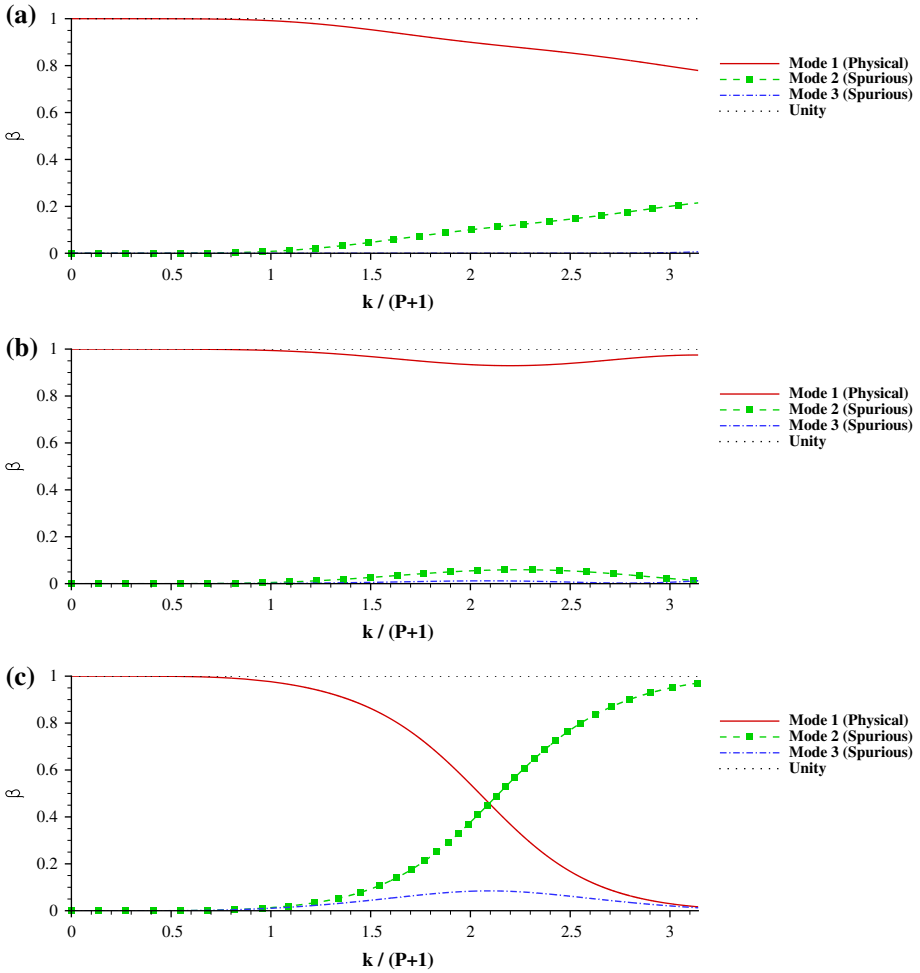
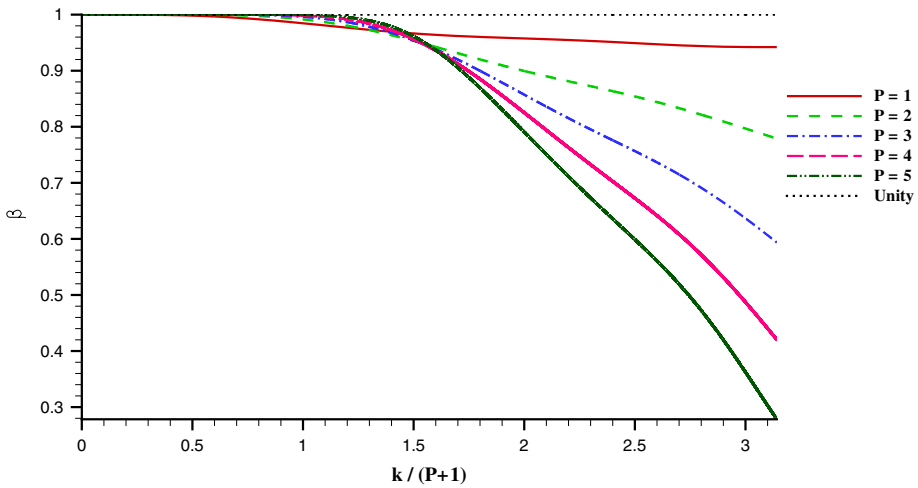


**Fig. 5** Effect of solution points on relative energies: Distribution of energy among numerical modes  $\beta_1$  to  $\beta_{P+1}$  for DG scheme via FR for  $P = 2$  on **a** Gauss–Legendre, **b** equidistant, and **c** Gauss–Lobatto solution points

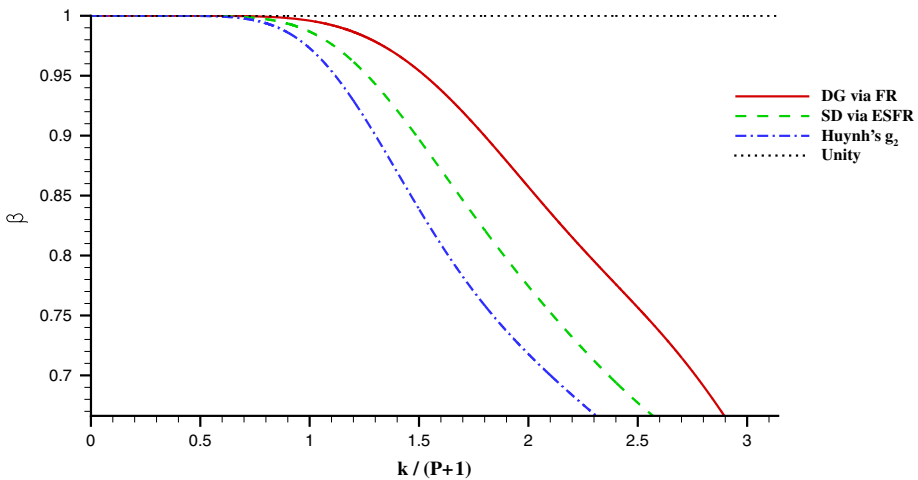
$$\beta_p = \frac{|\lambda_p|^2}{\sum_{q=1}^{P+1} |\lambda_q|^2} \tag{19}$$

Figure 5a plots  $\beta$  for the 3 eigenmodes for DG scheme via FR for  $P = 2$  at Gauss–Legendre solution points. We see that for low wavenumbers, the physical mode contains all the solution energy while at higher wavenumbers the fraction of energy in the spurious modes rises, eventually becoming a significant fraction near the Nyquist limit.

Huynh [11] proved that the eigenvalues of the FR eigensystem Eq. (14) are independent of the choice of solution points by showing that the corresponding Fourier matrices are similar. However, from Figs. 5b, c we see that the energy distribution changes significantly when the solution points are chosen to be equidistant or Gauss–Lobatto points respectively. While equidistant points do slightly better at preserving maximum energy in the physical mode,



**Fig. 6** Effect of polynomial order on relative energies: Fraction of energy retained in the physical mode  $\beta_1$  for DG scheme via FR for  $P = 1$  to 5 on Gauss–Legendre solution points



**Fig. 7** Effect of correction function on relative energies: Fraction of energy retained in the physical mode  $\beta_1$  for DG, SD and Huynh’s  $g_2$  scheme (via FR) for  $P = 2$  on Gauss–Legendre solution points

their use is still limited due to aliasing errors [15]. In the case of Gauss–Lobatto points, one notes the presence of a crossover point whereafter one of the spurious modes captures a higher fraction of energy than the physical mode.

Figure 6 plots  $\beta$  for the physical mode for DG scheme via FR for  $P = 1$  to 5 at Gauss–Legendre solution points. Here again, a competing effect can be observed with increase in polynomial order. While the point of departure from near unit energy fraction in the physical mode is pushed towards high normalized wavenumbers, the energy content for the highest wavenumbers decreases with increase in  $P$ . The dependence of energy content on the choice of correction function is relatively weaker as can be seen in Fig. 7 which plots  $\beta$  for the physical mode for the DG, SD and Huynh’s  $g_2$  correction functions.

### 2.6 Dispersion and Energy Distribution for Central Interface Fluxes

As can be seen from Eqs. (9), (10) and (14), the semi-discrete numerical dispersion relation is directly dependent upon the nature of the interface flux. While a fully upwinded flux is naturally admitted by the 1-D advection equation, results for a central flux ( $f^{int}(x_j) = (u_{j-1}^\delta(x_j) + u_j^\delta(x_j))/2$ ) have also been included for completion. The corresponding eigenvalue problem in this case can be written as

$$\frac{-2i}{k} \left( \mathbf{C}_0 + e^{-ik} \mathbf{C}_{-1} + e^{ik} \mathbf{C}_{+1} \right) \mathbf{v} = a^\delta \mathbf{v} \tag{20}$$

where

$$\begin{aligned} \mathbf{C}_0 &= \mathbf{D} - \frac{1}{2} \mathbf{g}_{\mathbf{L}, \xi} \mathbf{l}_{\mathbf{L}}^T - \frac{1}{2} \mathbf{g}_{\mathbf{R}, \xi} \mathbf{l}_{\mathbf{R}}^T \\ \mathbf{C}_{-1} &= \frac{1}{2} \mathbf{g}_{\mathbf{L}, \xi} \mathbf{l}_{\mathbf{R}}^T \\ \mathbf{C}_{+1} &= \frac{1}{2} \mathbf{g}_{\mathbf{R}, \xi} \mathbf{l}_{\mathbf{L}}^T \end{aligned} \tag{21}$$

We find that the imaginary parts of the numerical wavespeeds  $a_i^\delta$  are identically zero for all the numerical modes (physical as well as spurious) and for all correction functions. This result concurs with the theoretical analysis of Vincent et al.[14] wherein it was shown that the broken Sobolev norm of the type in Eq. (27) remains unchanged if a central flux is chosen. This also suggests that the only source of dissipation in the FR framework arises from the upwinding in the Riemann solve at each interface. Figure 8 plots the real part of the numerical wavespeed for the DG scheme recovered via FR for  $P = 2$  on Gauss–Legendre solution points. These are again in good agreement with the results of Hu et al.[27]. We see that for a significant fraction of the resolvable wavenumbers the physical mode exhibits a negative wavespeed. In fact, it is characterized by excessive dispersion for  $k/(P + 1) \geq 1.047$ . However, numerical results with a Gaussian initial condition (see Section 4.1.3 in [14]) suggest that central

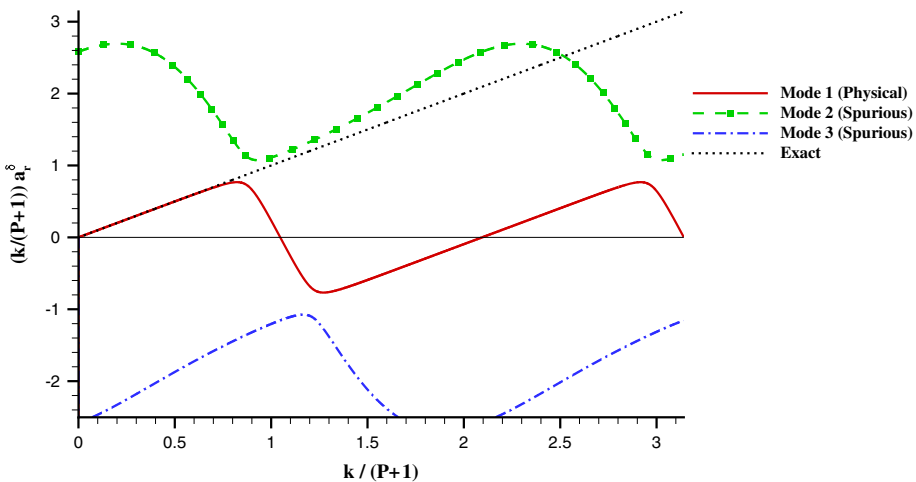


**Fig. 8** Effect of central flux on dispersion: Effective wavenumber  $k_{eff} = k a_r^\delta / (P + 1)$  of the numerical wavespeed for the 3 numerical modes for DG scheme via FR for  $P = 2$  when using a central flux. The imaginary part of the wavespeed is exactly zero

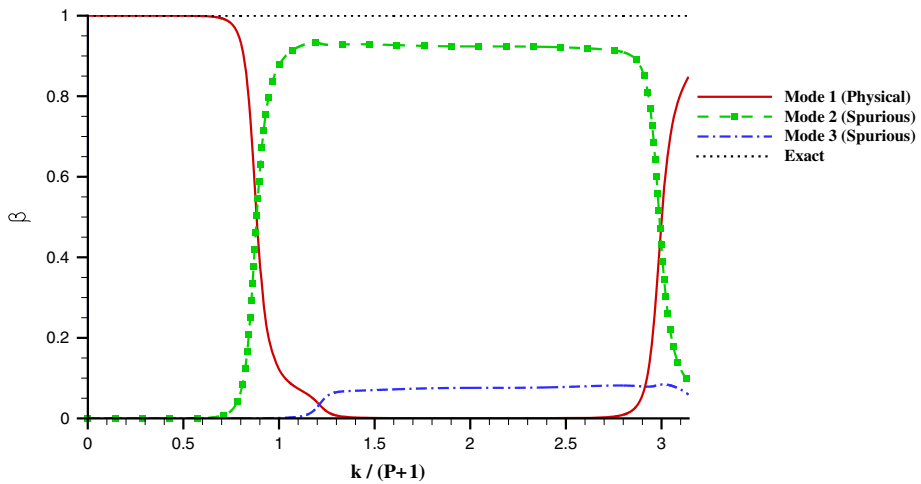


**Fig. 9** Effect of central flux on relative energies: distribution of energy among numerical modes  $\beta_1$  to  $\beta_{P+1}$  for DG scheme via FR for  $P = 2$  on Gauss–Legendre solution points when using a central flux

fluxes perform reasonably well even for long times. This can be understood from Fig. 9 by observing the partition of energy among the three numerical modes. For this case, we see that the fraction of energy contained in the physical mode falls rapidly beyond the point where it starts exhibiting large dispersion errors. In fact, one of the spurious modes receives the dominant share of energy beyond this point. While this spurious mode is highly dispersive for lower wavenumbers, it shows relatively small dispersion errors thereafter which causes the central flux to do relatively well on the whole.

### 3 Spectrally Optimal FR Schemes

In this section we utilize the results of Sect. 2 to propose a set of new FR schemes that provide minimum wave-propagation error for the range of resolvable wavenumbers. These schemes are obtained through optimal choices of correction function by solving a relevant minimization problem in the spectral space. Unlike spectrally optimal finite-difference schemes, the formal order of accuracy is retained to be the same ( $\mathcal{O}(h^{P+1})$ ) as those of regular FR schemes. As a simple first case, optimal ESFR schemes [14] are obtained by optimizing over the free parameter ‘ $c$ ’. Thereafter, the general problem of optimizing over the free zeros of the correction function is considered, and linearly stable, optimal schemes are recovered in the process.

#### 3.1 Wave Propagation Error and Constrained Minimization Problem

Conventionally, spectrally optimal finite-difference schemes [6, 23, 25] have been obtained by relaxing the formal order of accuracy in order to obtain free parameters that can be tuned to maximize the region over which the analytical dispersion relation is preserved. Since traditional explicit as well as implicit compact schemes had a central stencil, there was no added numerical dissipation and only dispersive errors had to be minimized. A direct approach [21] has been to minimize the absolute deviation of the numerical wavespeed from

the analytical wavespeed across the range of resolved wavenumbers  $\eta = \int_{k=0}^{\pi} |a^\delta - 1|^2 dk$ . However, owing to the upwinding present implicitly in the Riemann solve at each interface, FR schemes result in a negative imaginary part associated with numerical dissipation. An objective function of this form would not be suitable since it employs an algebraic weighting of the dispersive and dissipative errors that may lead to a biased optimum. Instead of prescribing weights for the two types of errors, it is convenient to select the error function directly as the error associated with wave propagation. Since the analytical form of the exact solution [Eq. (12)] and numerical solution [Eq. (13)] are available, we can express the error at time  $t$  as

$$\begin{aligned} |e(k, t)| &= |u(k, t) - u^\delta(k, t)| \\ &= \left| e^{ikj} \left( e^{ik(x-t)} - e^{ik(x-a^\delta t)} \right) \right| \\ &= |1 - e^{ik(1-a^\delta)t}| \end{aligned} \tag{22}$$

The time of error determination  $t$  can be chosen based on the characteristic time associated with the non-dimensionalization of the problem  $t_c = h/c = 1$ . This is the time required by the exact solution to travel one element width. For the present analysis, we are interested in schemes for long time integration that would provide low errors for propagation across the entire domain (which, for external flows in most engineering problems, is of the order of 100 grid points or more). For this reason, we have chosen  $t = 100 t_c$  so that  $\eta = \int_{k=0}^{\pi} |1 - e^{i 100k(1-a^\delta)}| dk$ .

An objective function for the FR optimization process can now be specified as the  $L_1$  error summed over all the  $P + 1$  modes weighted by their relative energy fractions, integrated over the range of resolvable wavenumbers

$$\eta = \frac{1}{(P + 1)^2} \sum_{p=1}^{P+1} \int_{k=0}^{(P+1)\pi} |1 - e^{i 100k(1-a_p^\delta(k))}| \beta_p(k) dk \tag{23}$$

where the factor of  $1/(P + 1)^2$  is used to normalize the error across polynomial order. The optimization problem with the stability criterion can be stated as follows

$$\begin{aligned} \min \quad & \eta(g(\xi)) \text{ given } P, \xi \\ \text{subject to} \quad & a_{p_i}^\delta(k) \leq 0 \quad \forall k \in [0, (P + 1)\pi], \quad p = 1, 2, \dots, P + 1 \end{aligned} \tag{24}$$

where  $g(\xi)$  is the correction function in the parent domain and  $\xi = [\xi_1, \xi_2, \dots, \xi_{P+1}]^T$  is the vector of solution points.

### 3.2 Spectrally Optimal Energy Stable FR Schemes (OESFR)

We begin by optimizing within the class of energy stable flux reconstruction (ESFR) schemes [14] that are linearly stable by construction. For ESFR schemes, the solution points are taken to be Gauss–Legendre points while the left and right boundary correction functions are defined as

$$\begin{aligned} g_L &= \frac{(-1)^P}{2} \left[ L_P - \left( \frac{\mu_P L_{P-1} + L_{P+1}}{1 + \mu_P} \right) \right] \\ g_R &= \frac{1}{2} \left[ L_P + \left( \frac{\mu_P L_{P-1} + L_{P+1}}{1 + \mu_P} \right) \right] \end{aligned} \tag{25}$$

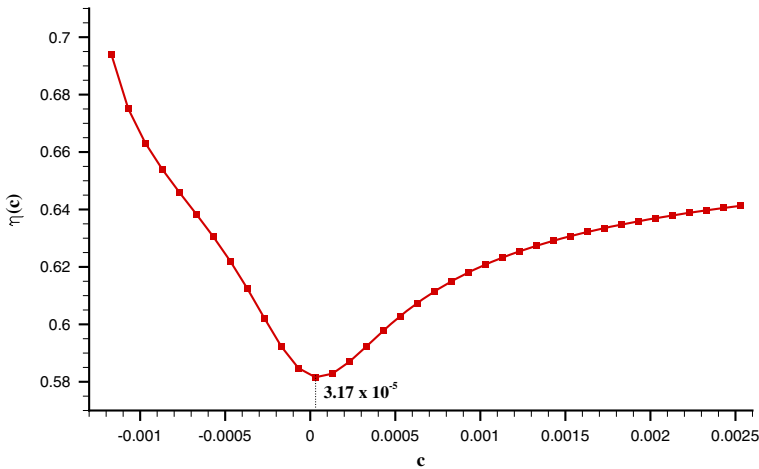


**Fig. 10** OESFR: Variation of the objective function with the ESFR parameter  $c$  for  $P = 3$  denoting the presence of a minimum close to the DG value of  $c = 0$

where

$$\mu_P = c \frac{2P + 1}{2} \left( \frac{(2P)!}{2^P (P)!} \right)^2 \tag{26}$$

Here,  $L_P$  is the Legendre polynomial of degree  $P$ , and  $c \in [c_-, \infty)$  is the free parameter of the scheme. The left bound,  $c_-$ , is the lowest value of  $c$  that yields a legitimate energy norm which, for the non-dimensionalization defined in Sect. 2.1, is of the form

$$\|u^\delta\|_{P, 2} = \left[ \sum_{j=1}^{n_{el}} \int_{\Omega_j} (u_j^\delta)^2 + \frac{c}{2} \left( \frac{\partial^P u_j^\delta}{\partial x^P} \right)^2 dx \right]^{1/2} \tag{27}$$

The DG scheme is recovered from ESFR by choosing  $c = 0$ . The choice of  $c = c_+$  yields the scheme that offers the highest CFL limit for a given polynomial order. Optimal ESFR schemes (OESFR) can be obtained by optimizing over  $c$  for any given  $P$ . The minimization problem is unconstrained as the family is guaranteed to be linearly stable.

As noted in [30], we see that as  $c$  is increased beyond 0, a competing effect is observed regarding the point of departure from the exact dispersion relation. While the departure of the real component of wavespeed gets pushed to higher  $k$ , that for the imaginary component gets pulled to lower  $k$ . This suggests the presence of a minimum of the error close to  $c = 0$ . Figure 10 plots the variation of the objective function against  $c$  for  $P = 3$ . The objective function is very well behaved and records a discernible minimum close to  $c = 0$  as expected. This optimal value along with the value of the objective function is tabulated in Table 1. The real and imaginary components of the wavespeed for the OESFR scheme are plotted in Fig. 11a, b for  $P = 4$  and Fig. 12a, b for  $P = 5$ . These figures have been discussed in detail in the next section for the sake of comparison.



**Table 1** Objective function (relative to DG) and internal zeros for the OESFR and OFR schemes

P	$\frac{\eta_{OESFR}}{\eta_{DG}}$	$\frac{\eta_{OFR}}{\eta_{DG}}$	$c_{OESFR}$	$\{\zeta_{OESFR}\}$	$\{\zeta_{OFR}\}$
1	0.9997	0.9997	$8.40 \times 10^{-3}$	{-0.324947954}	{-0.324947954}
2	0.9169	0.9168	$5.83 \times 10^{-4}$	{-0.687046768, 0.294921433}	{-0.683006984, 0.302192636}
3	0.9279	0.9183	$3.17 \times 10^{-5}$	{-0.820508633, -0.174051445, 0.580238407}	{-0.839877076, -0.202221672, 0.518569180}
4	0.8806	0.7658	$9.68 \times 10^{-7}$	{-0.883539936, -0.437806887, 0.177747440, 0.725821574}	{-0.856985048, -0.447652425, 0.180019034, 0.638102912}
5	0.8497	0.7216	$1.02 \times 10^{-8}$	{-0.919029563, -0.598291572, -0.115071988, 0.398821159, 0.806299103}	{-0.897887439, -0.577293821, -0.101190260, 0.354120544, 0.760380824 }

### 3.3 Spectrally Optimal General FR Schemes (OFR)

A general form of the correction function on the left boundary can be expressed using the internal zeros of the correction polynomial

$$g_L(\xi) = \prod_{q=1}^P \frac{(\xi - \zeta_q)(\xi - 1)}{1 + \zeta_q} \quad (28)$$

which ensures that the function is unity on the left boundary. The solution space of free zeros  $\langle \zeta \rangle = \{\zeta_1, \zeta_2, \dots, \zeta_{P+1}\}$  is of dimension  $P$  and recovers the ESFR family as a semi infinite contour beginning at the set of zeros corresponding to the ESFR scheme with  $c = c_-$ . The most general optimal FR schemes (OFR) can be obtained by minimizing over  $\langle \zeta \rangle$  subject to the constraint that the resulting scheme is linearly stable. The resulting optimization problem is solved using an interior-point method [32,33] with the help of MATLAB’s optimization toolbox [34] and is stiff in that the constraints are satisfied only within subsets of much lower dimension. This made a grid search seeding approach [35] infeasible as the initial guesses usually violated the constraints. In order to circumvent this issue, the initial guess points were taken to be the zeros of the corresponding OESFR schemes. Hence, while the resulting solutions might not be globally optimal, the results that follow suggest them to be locally optimal at the least.

Table 1 enlists the internal zeros of the OFR correction function along with the minimum of the objective function. For  $P = 1$ , the OFR optimization process converges to the zeros of the OESFR correction function, which is expected owing to a single degree of freedom. For  $P \geq 2$ , the optimization process converges to zeros that are not traced by the ESFR family. Since the constraint is strictly satisfied, we obtain linearly stable FR schemes that have minimum wave propagation error. The real and imaginary components of the wavespeed for the OFR scheme are plotted in Fig. 11a, b for  $P = 4$  and Fig. 12a, b for  $P = 5$ . The

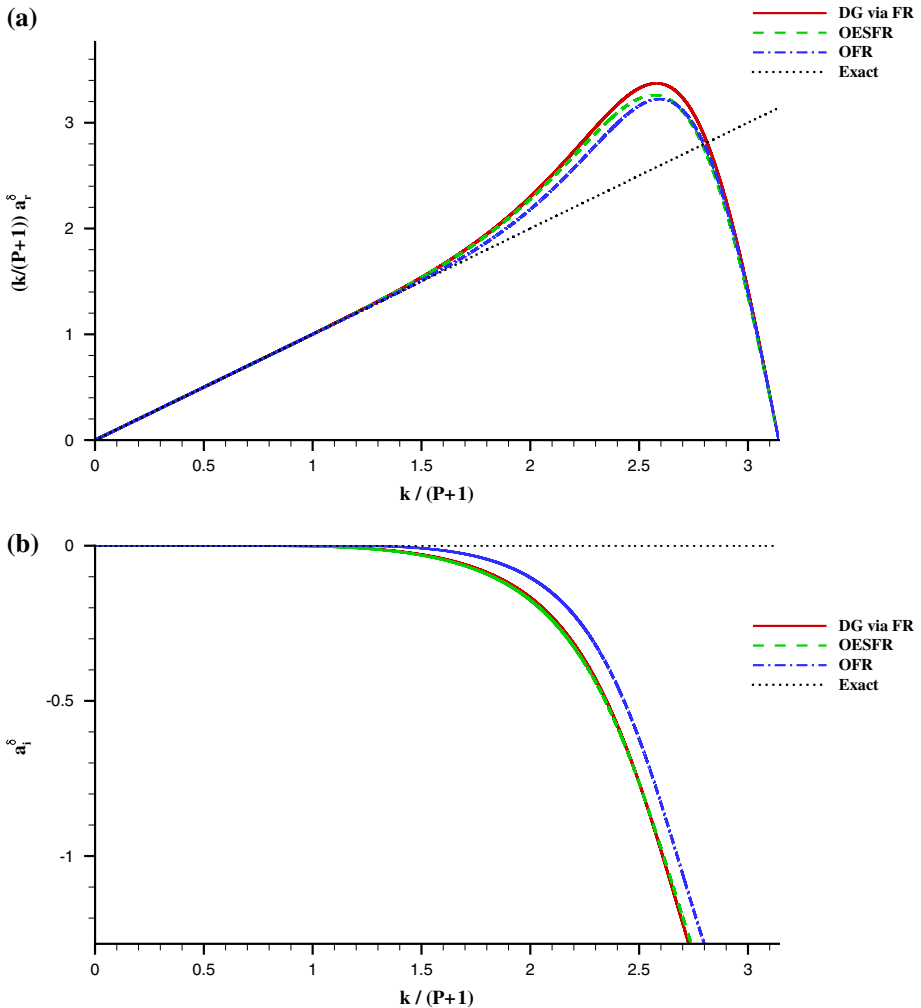


**Fig. 11** Optimal schemes: **a** effective wavenumber  $k_{eff} = k a_r^\delta / (P + 1)$  and **b** imaginary part  $a_i^\delta$  of the numerical wavespeed for the physical mode for DG, OESFR and OFR schemes for  $P = 4$ . Note that all three schemes are of the same formal order

contrast between OFR and OESFR or DG grows with polynomial order due to the increase in degrees of freedom.

Figure 13a, b plot the left boundary correction functions for the DG, OESFR and OFR schemes for  $P = 4, 5$  respectively. We note that the zeros of the OFR scheme are located in a manner that tends to minimize the deviation of the function from zero. This can be expected from Huynh’s [11] observation that correction functions tend to approximate zeros in the interior of the domain.

A quantitative measure of the fraction of the spectrum along which the dispersion relation is approximately preserved can be expressed in the form of resolving efficiency of the physical mode defined by Lele in [6]

$$e_1 = \frac{k_f}{(P + 1)\pi} \tag{29}$$

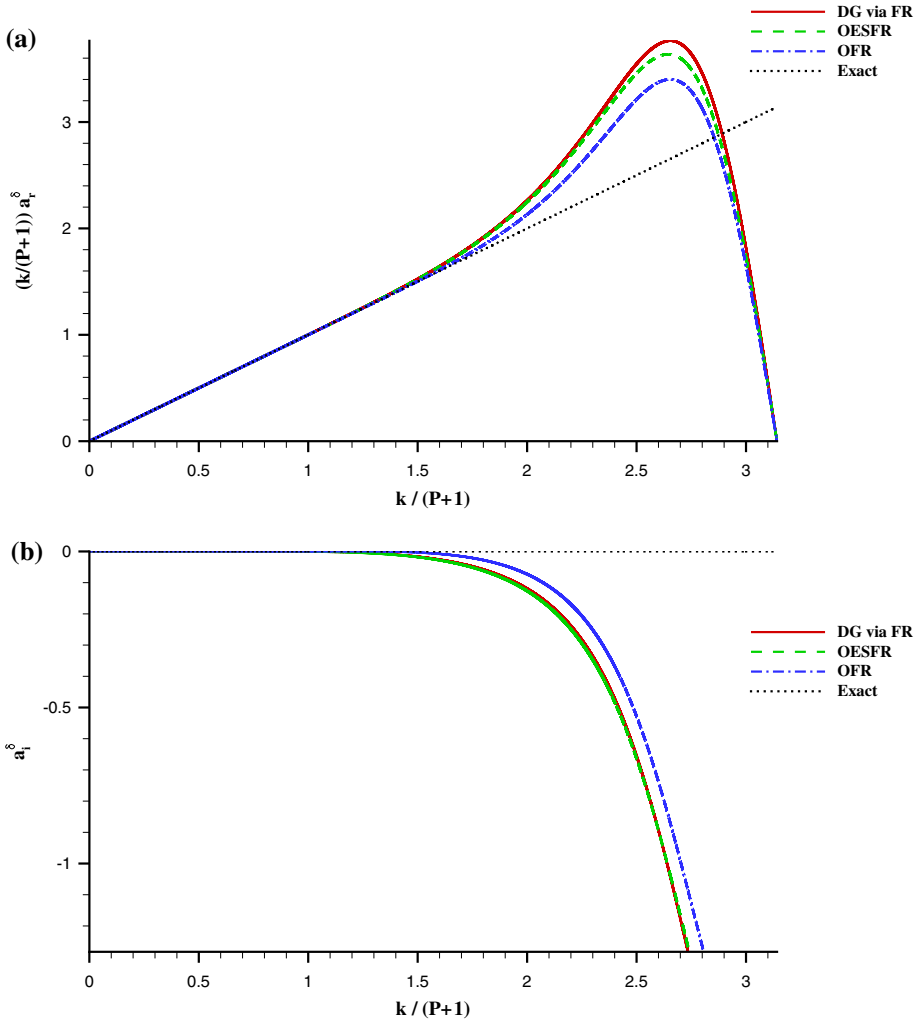


**Fig. 12** Optimal schemes: **a** effective wavenumber  $k_{eff} = k a_r^\delta / (P + 1)$  and **b** imaginary part  $a_i^\delta$  of the numerical wavespeed for the physical mode for DG, OESFR and OFR schemes for  $P = 5$ . Note that all three schemes are of the same formal order

where  $k_f$  is such that

$$|a^\delta(k) - 1| \leq \varepsilon, \quad \text{for } k \leq k_f \tag{30}$$

Table 2 compares the resolving efficiencies of the DG, OESFR, OFR and  $c_+$  [30] schemes for  $P = 3$  to 5. For  $P \leq 2$ , as the OFR scheme converges to the OESFR scheme, which in turn is only marginally better than DG, the resolving efficiencies for all three schemes are identical. However for  $P > 2$ , the OFR scheme provides higher resolution for either measure of the resolving efficiency. An improvement of about 20% is achieved through the use of OFR over DG for  $P = 4, 5$ . On the other hand, the  $c_+$  scheme suffers from a poor resolving power due to excessive dissipation. In fact, from Table 2 we see that the 4th order OFR scheme provides similar resolution to the 6th order  $c_+$  scheme. Note that the FR scheme of polynomial order  $P$  is formally  $P + 1$  order accurate.

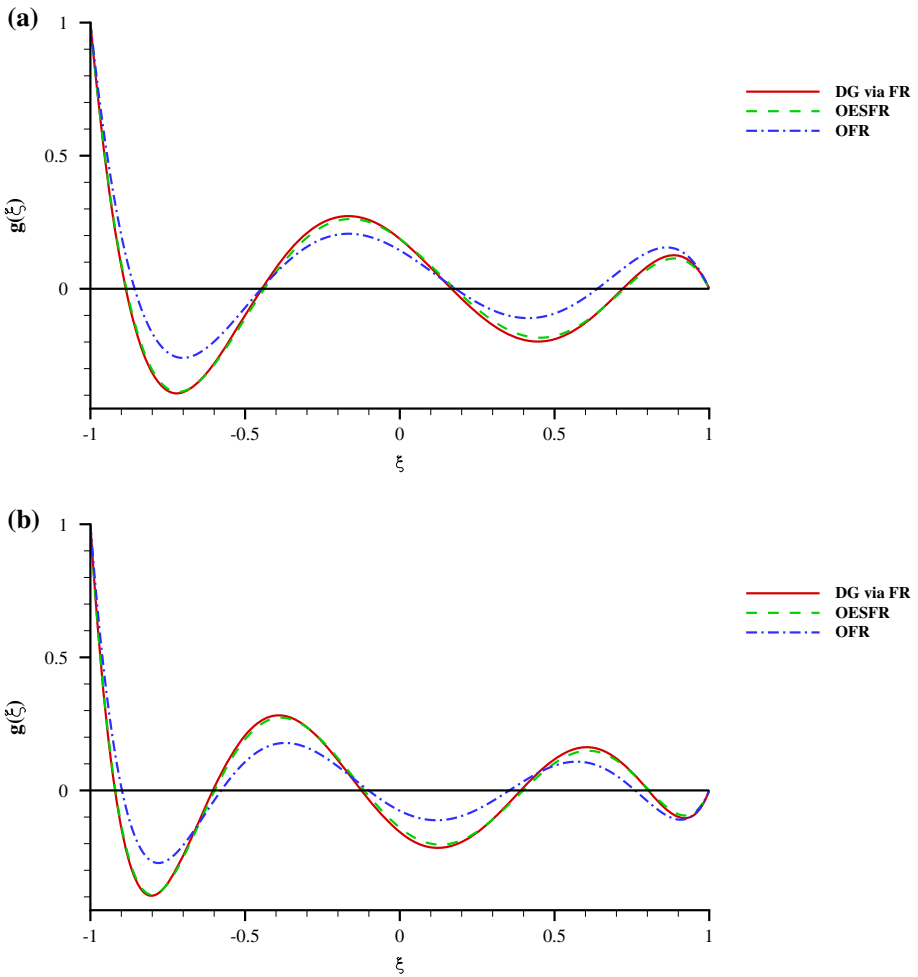


**Fig. 13** Left boundary correction functions for DG, OESFR and OFR schemes for **a**  $P = 4$  and **b**  $P = 5$

**Table 2** Resolving efficiency  $e_1$  for  $\varepsilon = 0.01, 0.001$  for DG, OESFR, OFR and  $c_+$  schemes

P	$\varepsilon = 0.01$				$\varepsilon = 0.001$			
	DG	OESFR	OFR	$c_+$	DG	OESFR	OFR	$c_+$
1	0.145	0.145	0.145	—	0.066	0.066	0.066	—
2	0.263	0.263	0.263	0.128	0.160	0.160	0.160	0.070
3	0.339	0.339	0.352	0.228	0.233	0.233	0.249	0.149
4	0.391	0.391	0.477	0.300	0.287	0.287	0.409	0.214
5	0.428	0.428	0.511	0.351	0.328	0.328	0.444	0.264

It is interesting to compare the resolving efficiency of the OFR schemes with standard Padé type compact finite difference schemes. Since the time complexity of the 1-D FR formulation is  $\mathcal{O}(n_{el}, P^2)$  for large  $n_{el}$ ,  $P$  and  $\mathcal{O}(P)$  for moderate  $P$ , it is consistent to compare against

**Table 3** Limiting CFL values for the DG, OESFR, OFR and  $c_+$  schemes for RK44 and RK45

P	RK44				RK45			
	DG	OESFR	OFR	$c_+$	DG	OESFR	OFR	$c_+$
1	0.464	0.470	0.470	–	0.679	0.686	0.686	–
2	0.235	0.238	0.241	0.688	0.352	0.356	0.361	0.864
3	0.139	0.148	0.126	0.376	0.220	0.224	0.191	0.473
4	0.100	0.103	0.108	0.245	0.152	0.158	0.164	0.311
5	0.068	0.076	0.085	0.174	0.110	0.117	0.128	0.223

**Table 4** Limiting CFL values for the DG, OESFR, OFR and  $c_+$  schemes for RK33 and SSPRK(4,3)

P	RK33				Optimal SSPRK(4,3)		
	DG	OESFR	OFR	$c_+$	DG	OESFR	OFR
1	0.411	0.415	0.415	–	0.594	0.601	0.601
2	0.210	0.212	0.210	0.623	0.308	0.311	0.316
3	0.130	0.133	0.109	0.334	0.191	0.196	0.166
4	0.080	0.091	0.095	0.212	0.133	0.138	0.144
5	0.061	0.068	0.074	0.149	0.098	0.101	0.112

Note that the  $c_+$  scheme [30] has been derived only for RK3, RK44 and RK45

**Table 5** Numerical test cases employed in Sect. 5

Case	Schemes	P	Soln. pts.	Grid	Initial condition
1	DG, OESFR, OFR, $c_+$	5	Gauss–Legendre	Uniform	$e^{-38.6x^2}$
2	DG, OESFR, OFR, $c_+$	5	Gauss–Legendre	Uniform	$e^{-0.1x^2} \cos(3\pi x)$
3	DG, OESFR, OFR, $c_+$	5	Gauss–Legendre	Non-uniform	$e^{-38.6x^2}$
4	DG	2	Gauss–Legendre, Equidistant, Gauss–Lobatto	Uniform	$e^{-9.64x^2}$

compact difference schemes that are at maximum tridiagonal in structure. Table III in [6] lists the resolving efficiencies of 2nd order explicit, 4th order explicit and implicit, 6th order explicit and implicit and 8th order implicit difference schemes, all of which have linear time complexity in evaluating the derivative. On comparing, we note that the OFR scheme provides significantly higher resolution than the explicit difference schemes of the same order for either efficiency measure. In comparison to the implicit difference schemes, the OFR scheme provides similar resolution for  $\varepsilon = 0.01$  but a higher resolution for  $\varepsilon = 0.001$ . In fact, for  $\varepsilon = 0.001$ , the 6th order OFR scheme provides similar resolution to the 8th order implicit compact difference scheme.

#### 4 Time Integration and CFL Restriction

In this section, we determine CFL restrictions for the proposed schemes and compare them with existing FR schemes. In the process, the numerical operator  $\frac{d^{\delta}}{dt}$  is expanded for the

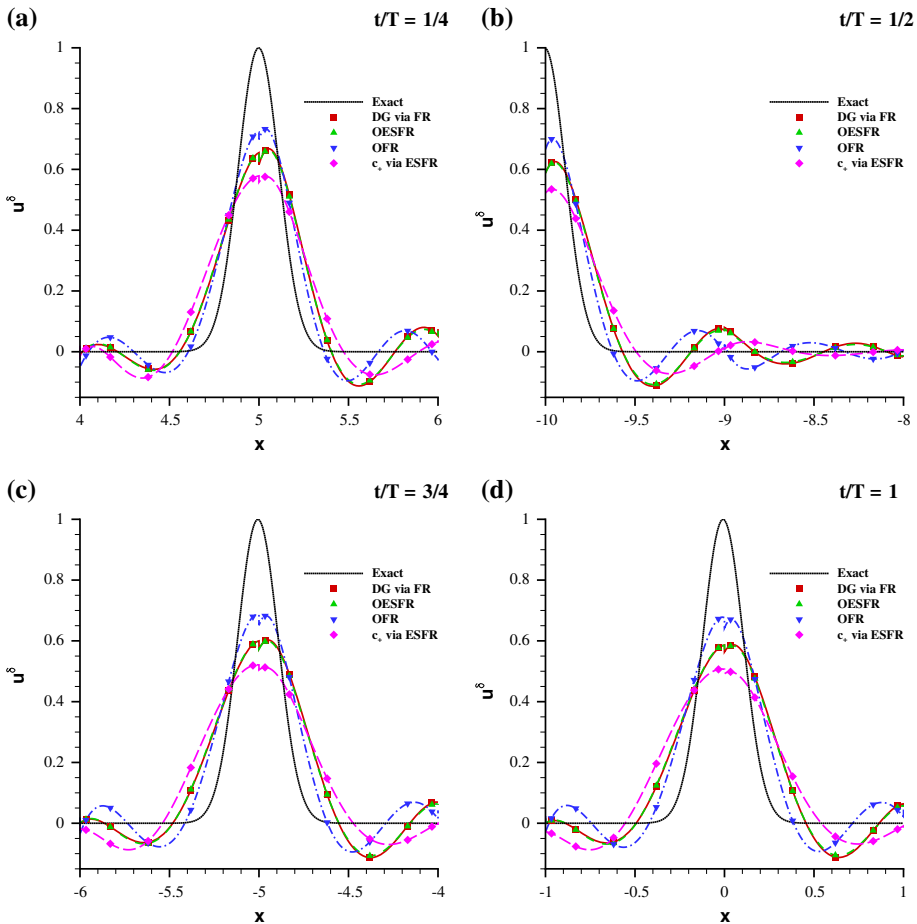


**Fig. 14** Case 1: Snapshots of the numerical solution for the DG, OESFR, OFR and  $c_+$  schemes at intervals of a quarter-period

case of a general N-stage explicit Runge Kutta type scheme which modifies the eigenvalue problem in Eq. (14). The new eigenvalue problem represents the numerical dispersion relation for the fully-discrete form of the FR update.

#### 4.1 Multi-stage time Scheme and Fully-Discrete Dispersion Relation

The semi-discrete dispersion relation Eq. (14) assumed exact integration in time. However, during an actual numerical update, the time-derivative operator  $\frac{d^\delta}{dt}$  in Eq. (9) is numerically approximated. The update equation can be rewritten using the Eq. (13) as

$$\frac{d^\delta}{dt} \mathbf{u}_j^\delta = \mathbf{Q} \mathbf{u}_j^\delta(t) \tag{31}$$

where  $\mathbf{Q} = -2(\mathbf{C}_0 + e^{-ik}\mathbf{C}_{-1})$ . Owing to the differential form of FR, Eq. (31) can be updated using a general N-stage explicit Runge Kutta type scheme

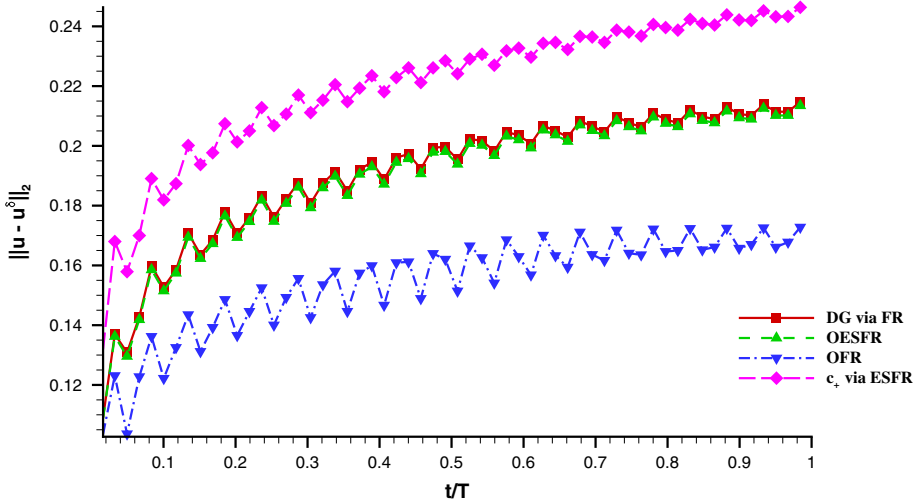


**Fig. 15** Case 1: Evolution of  $L_2$  norm of the error for the DG, OESFR, OFR and  $c_+$  schemes

$$\begin{aligned}
 \mathbf{u}_j^\delta(t + \Delta t) &= \left( \sum_{n=0}^N \alpha_n \frac{(\mathbf{Q}\Delta t)^n}{n!} \right) \mathbf{u}_j^\delta(t) \\
 &= \mathbf{R} \mathbf{u}_j^\delta(t)
 \end{aligned}
 \tag{32}$$

where  $\Delta t$  is the numerical time step,  $\alpha$  is the vector of coefficients of the RK scheme and  $N$  is the number of stages. The presence of a numerical time integration operator modifies the associated eigenvalue problem to provide the fully-discrete numerical dispersion relation as

$$\mathbf{R} \mathbf{v} = e^{-i k a^\delta \Delta t} \mathbf{v}
 \tag{33}$$

Note that, since  $e^{-i k a^\delta \Delta t} = 1 - i k a^\delta \Delta t + \mathcal{O}(\Delta t^2)$  and  $\mathbf{Q} = -i k \mathbf{M}$ , Eq. (33) reduces to Eq. (14) in the limit  $\Delta t \rightarrow 0$  where only the first order terms survive.

### 4.2 CFL Restriction

Equation (33) represents a discrete linear dynamical system whose stability criterion can be expressed in terms of the spectral radius  $\rho$

$$\rho(\mathbf{R}) \leq 1 \quad \forall k \in [0, (P + 1)\pi]
 \tag{34}$$

Table 3 provides limiting CFL values for the DG, OESFR, OFR and  $c_+$  schemes for the standard 4 stage, 4th order RK scheme RK44 and the enhanced stability 5 stage, 4th order scheme RK45 [36]. The corresponding values for  $3^{rd}$  order schemes including the 3 stage standard RK scheme RK33 and the optimal four stage, low storage, strong-stability-preserving scheme SSPRK(4,3) of Kubatko et al. [37] have also been provided in Table 4. We begin by noting that the CFL limit for the OESFR scheme is higher than DG via FR for all polynomial orders. This is expected as the CFL limit increases with  $c$  from  $c = 0$  to  $c = c_+$  as shown in [30] and that the optimal  $c$  value for OESFR was found to be greater than 0. We also note that the CFL limit for the OFR scheme compares well to that for the DG scheme, thereby suggesting that the additional accuracy obtained through tuning of the zeros of the correction function does not come at the expense of linear stability. While the  $c_+$  scheme has a much higher CFL

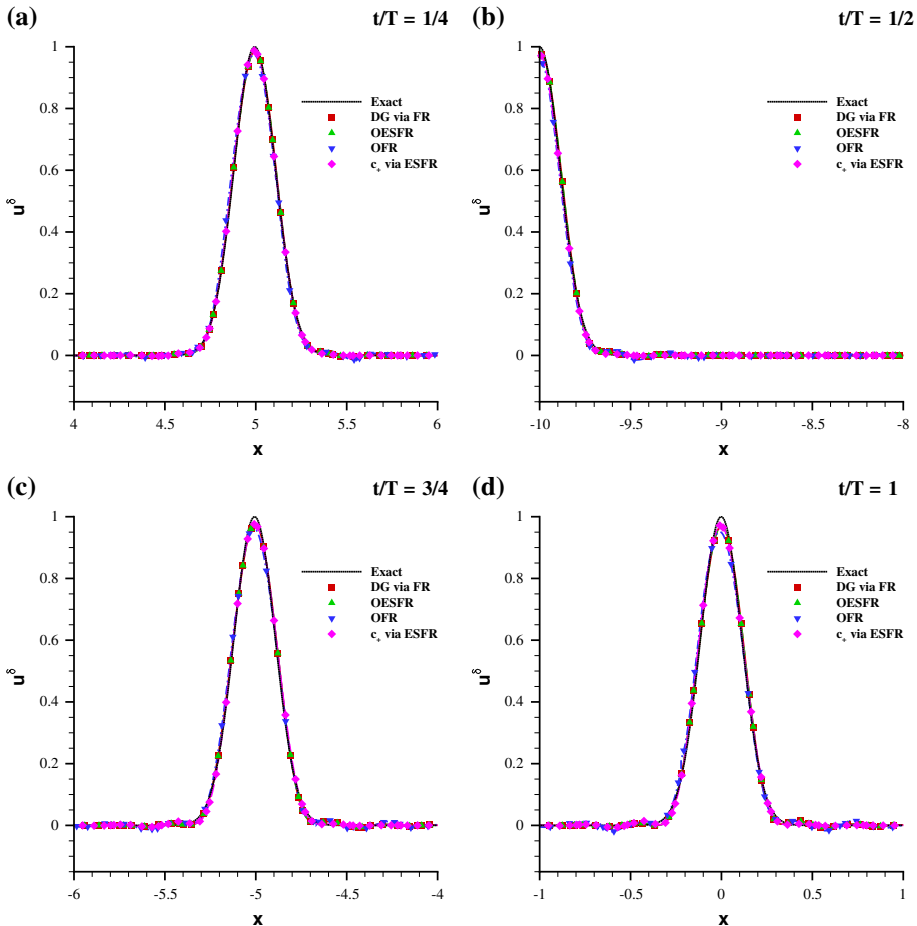


**Fig. 16** Case 1 with refined grids: Snapshots of the numerical solution for the DG, OESFR schemes using 61 elements, OFR scheme using 45 elements and  $c_+$  scheme using 76 elements at intervals of a quarter-period

limit as expected, it suffers from significantly larger dispersion errors that makes it ill-suited for wave propagation problems. The next section provides numerical examples outlining this aspect.

## 5 Numerical Test: Linear Advection of a Wave Packet

This section presents the results of numerical tests to validate the analytical expectations derived in the previous sections. Since a salient feature of the FR formulation is its applicability to complex geometries with non-uniform grids, it is important to show that the advantage of using the proposed schemes that have been optimized for a uniform grid is retained even on arbitrarily stretched non-uniform grids. Additionally, a test case is included to demonstrate the importance of choice of solution points even for linear fluxes. Table 5 lists the various cases that have been investigated in this study.



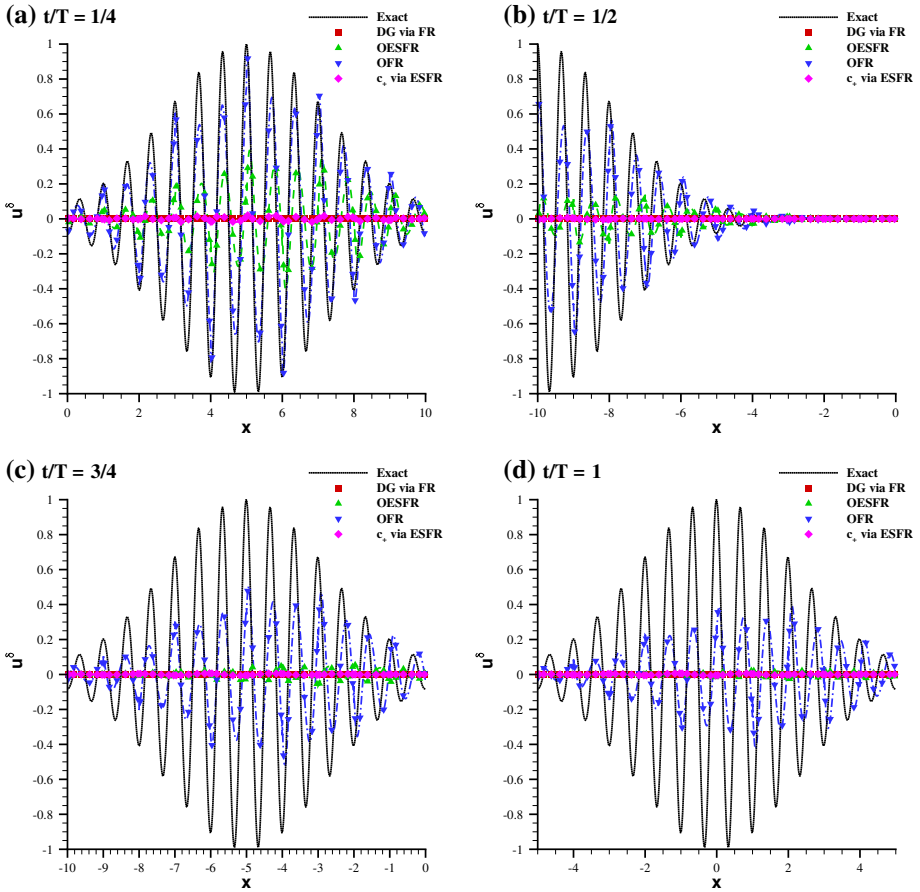


**Fig. 17** Case 2: Snapshots of the numerical solution for the DG, OESFR, OFR and  $c_+$  schemes at intervals of a quarter-period

### 5.1 Case 1: Advection of a Sharp Gaussian on a Uniform Grid

The first case deals with linear advection of a Gaussian on a uniform grid. The non-dimensional length and velocity are the same as defined in Sect. 2.1. The domain is defined on  $[-10, 10]$  and the number of elements is taken to be 20 which conveniently normalizes the grid spacing to unity. The polynomial order  $P$  is 5 and the solution points within each element are chosen to be the Gauss–Legendre points in the parent domain. The initial condition  $u_0(x) = e^{-38.6x^2}$  is a Gaussian with zero mean, unit peak and variance  $\sigma^2 = 1/(77.2)$  which is chosen so that  $\hat{u}_0(k = (P + 1)\pi)/\hat{u}_0(k = 0) = 0.1$ , where  $(\hat{u}_0)$  denotes the Fourier transform of  $u_0(x)$ . This ensures that the initial condition spans the entire range of resolvable wavenumbers with 10% amplitude at the Nyquist limit. This problem is solved using the DG scheme as reference, the proposed OESFR and OFR schemes, and the  $c_+$  scheme. For all schemes, the CFL number is chosen to be half of the maximum allowable CFL number for the DG scheme. The boundary conditions are taken to be periodic and the solution is made to advect for a full period  $T = |\Omega| = 20$ . Figure 14 provides snapshots of the numerical

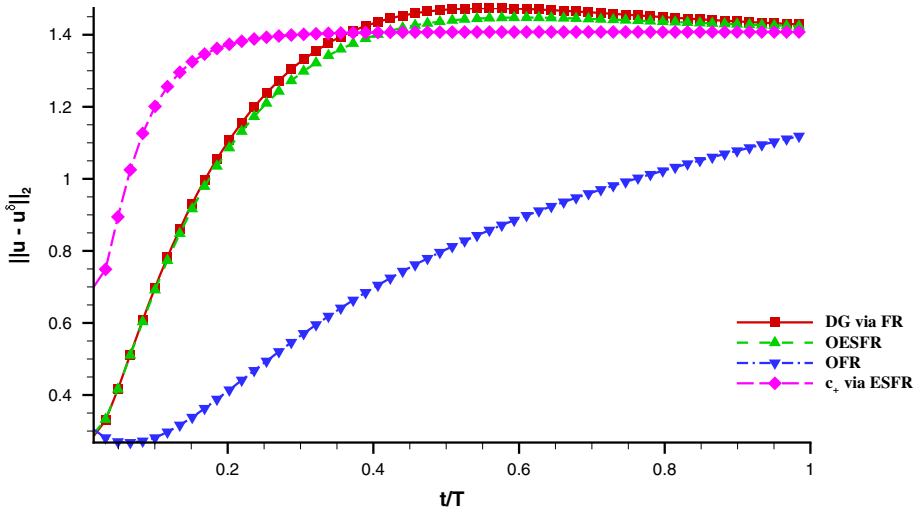


**Fig. 18** Case 2: Evolution of  $L_2$  norm of the error for the DG, OESFR, OFR and  $c_+$  schemes

solution for the employed schemes at intervals of a quarter period  $T/4$ . The exact solution is included for reference. As expected from optimality in spectral space, the OFR scheme provides the least dissipated solution, followed by the OESFR scheme which almost overlaps with the DG solution. This suggests that optimization within the ESFR family provides little advantage over the DG scheme. The  $c_+$  scheme which had the highest stability limit is the most dissipative in this set of schemes. A quantitative comparison among the schemes can be carried out through the standard  $L_2$  function norm

$$\|u - u^\delta\|_2 = \left( \sum_{j=1}^{n_{el}} \int_{\Omega_j} (u(x \in \Omega_j) - u_j^\delta(x))^2 dx \right)^{1/2} \tag{35}$$

Figure 15 compares the evolution of the  $L_2$  error for the employed schemes. As expected, the error for all of the schemes rises with time due to the dispersion and dissipation errors committed at each update. The small scale periodicity in the error is a consequence of the piecewise nature of the FR solution. The errors are lower when the Gaussian peak is located at the interfaces between elements and higher when the peak is centered within any element. The uniformity in the periods is on account of the uniformity in the grid. Here again, we see that the OFR scheme provides a considerably lower error than the DG scheme while the  $c_+$  scheme provides larger ones at all times during the period.

The resolving capabilities of these schemes can alternatively be compared by the grid resolution that each of them requires to accurately advect this steep Gaussian for a full period. Such a measure of resolution is directly related to the resolving efficiency  $e_1$  evaluated in Sect. 3.3. From Table 2, we note that for the DG (via FR) scheme, for  $P = 5$ , to accurately resolve the wavelength at the Nyquist limit for the grid in Case 1, we require  $20/e_1|_{\varepsilon=0.001, P=5}^{DG} \simeq 61$  elements. Similarly, for the OFR scheme we require 45 elements, and for the  $c_+$  scheme, we require 76 elements. Note that there would still be some numerical error as the spectrum of the initial condition extends beyond the original Nyquist limit by construction. Figure 16 provides snapshots of the numerical solution for the employed schemes at intervals of a

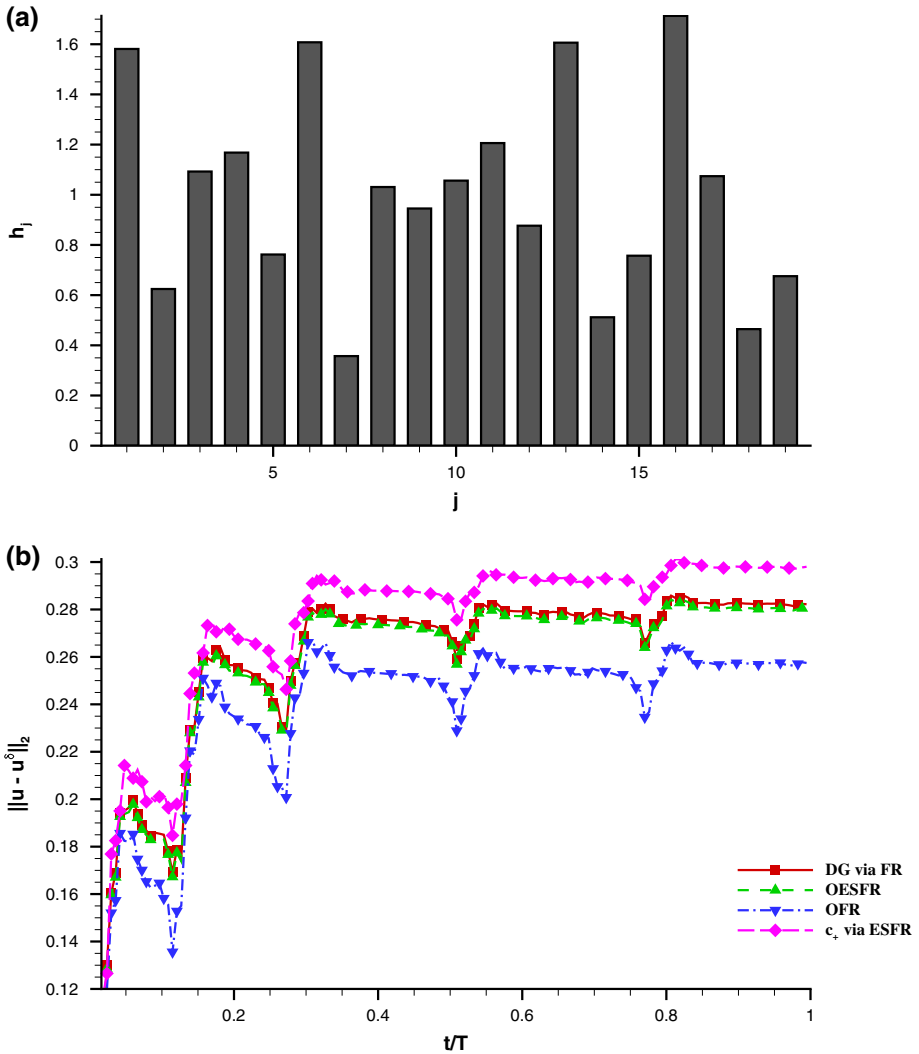


**Fig. 19** Case 3: **a** Variation of element size  $h_j$  across the perturbed, non-uniform grid, **b** Evolution of  $L_2$  norm of the error for the DG, OESFR, OFR and  $c_+$  schemes

quarter period  $T/4$  where the number of elements for each scheme is chosen as described above. As can be seen, each of the schemes resolve the Gaussian reasonably well through their respective grids. In this case, the advantage received by using the spectrally optimal OFR scheme is that it provides accurate solutions at coarser grids.

### 5.2 Case 2: Advection of a High Wavenumber Packet on a Uniform Grid

The second case is chosen to highlight the advantage of using the proposed scheme in advecting moderately high wavenumber components. For this reason, the initial condition  $u_0 = e^{-0.1x^2} \cos(3\pi x)$  is a packet centered in the spectral space about  $k = (P + 1)\pi/2$ , half

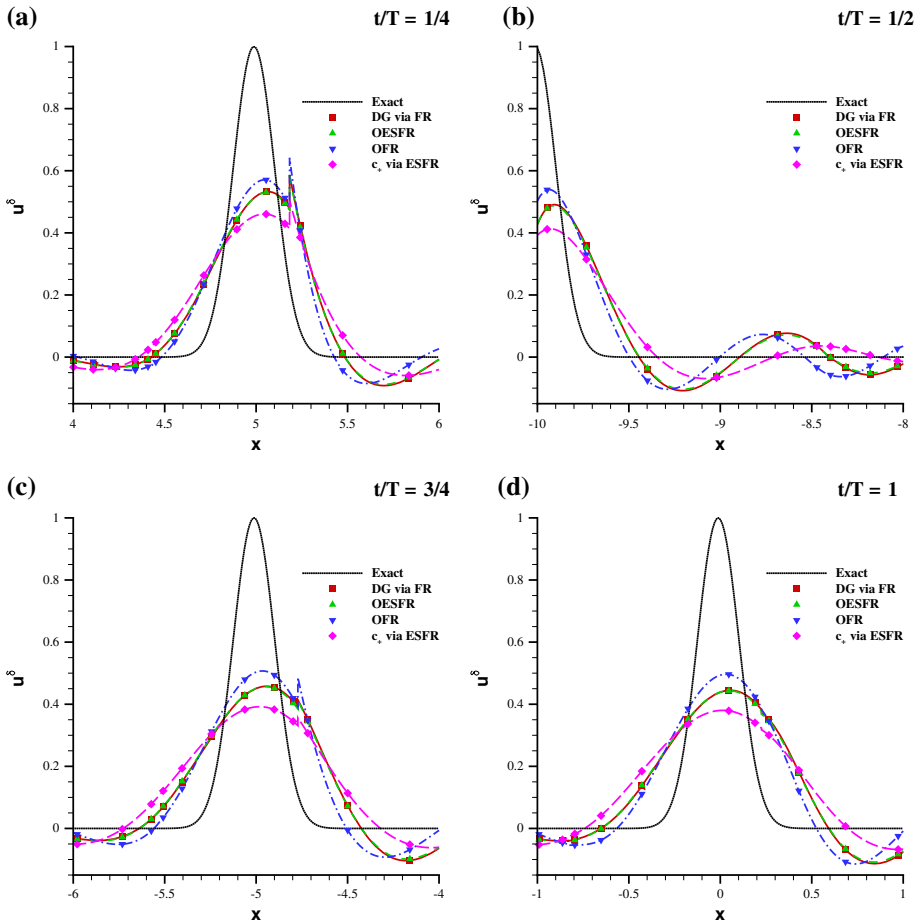


**Fig. 20** Case 3: Snapshots of the numerical solution for the DG, OESFR, OFR and  $c_+$  schemes at intervals of a quarter-period

of the Nyquist limit. The remaining parameters of the case are identical to the previous one. Figure 17 provides snapshots of the numerical solution for the four schemes. We see that even in one quarter of the period, the excessive dissipation in the  $c_+$  scheme has completely dissipated the solution, while the DG and OESFR schemes also cause substantially larger dissipation as well as dispersion errors than the OFR scheme. At the end of one period, the DG and OESFR solutions have decayed completely. Figure 18 compares the evolution of the  $L_2$  error demonstrating the flattening of the norm once the solution has decayed. Note that the apparently small improvement achieved via optimization results in a significant reduction in physical error.

### 5.3 Case 3: Advection of a Sharp Gaussian on a Non-uniform Grid

Having confirmed the advantage of optimality on uniform grids, we now deal with the case of a randomly stretched non-uniform grid. The grid for this case is constructed by randomly perturbing the uniform grid in Case 1,  $x'_j = x_j + 0.99h\theta$ , where  $x_j$  is the left interface location

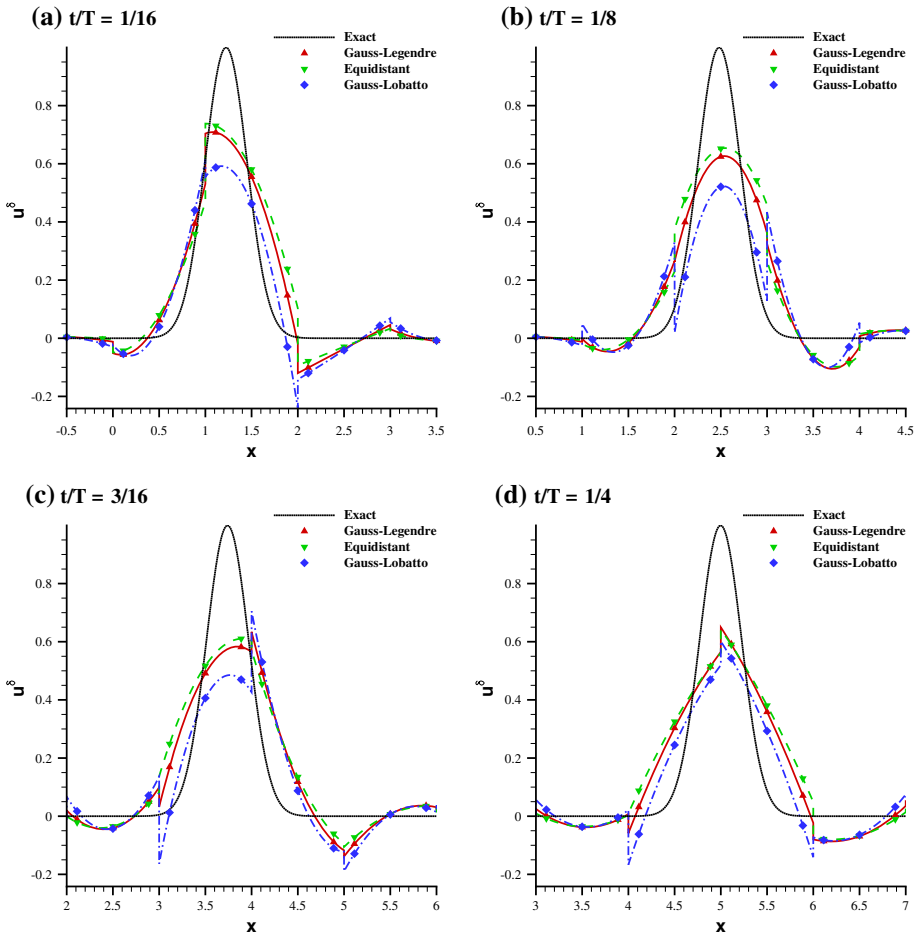


**Fig. 21** Case 4: Snapshots of the numerical solution for the DG scheme on Gauss–Legendre, equidistant and Gauss–Lobatto points at intervals of a sixteenth-period

of the  $j$ th element and  $\theta$  is uniformly distributed in  $[0, 1]$ . A bar chart of the resulting element widths is given in Fig. 19a. All other parameters, including the initial condition are identical to the first case. Figure 20 provides similar plots as for the uniform grid case. The results are qualitatively similar but the difference between the schemes is lesser than before. The evolution of the error norm in Fig. 19b is directly affected by the non-uniformity in the grid. The solution suffers large errors every time the Gaussian has to pass through an element of relatively large width. While the OFR scheme still provides lower errors than the other FR schemes, the improvement is limited by the presence of highly stretched elements.

#### 5.4 Effect of the Choice of Solution Points

Finally, we consider a case to examine the effect of the choice of solution points. The polynomial order is taken to be 2 in order to complement the analysis provided in Sect. 2.5. The domain is taken to be the same as before, discretized by a uniform grid. As in Case 1, the

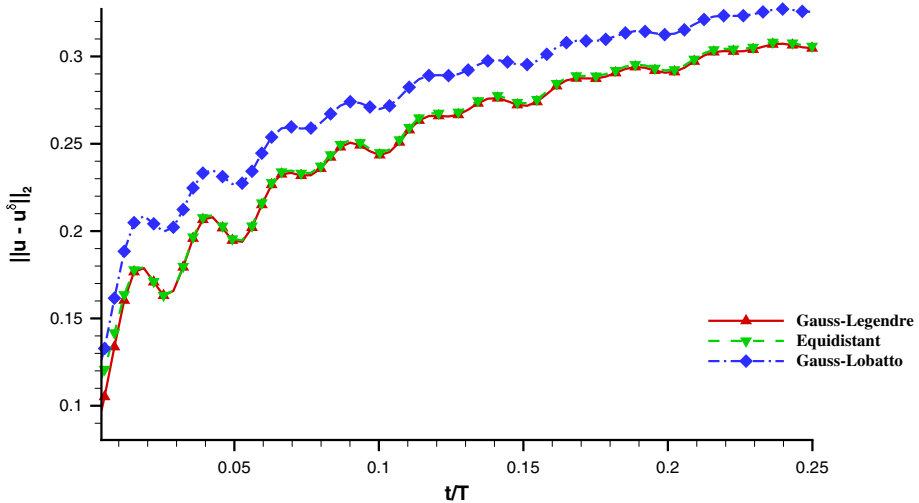


**Fig. 22** Case 4: Evolution of  $L_2$  norm of the error for the DG scheme via FR on Gauss–Legendre, equidistant and Gauss–Lobatto points

initial condition  $u_0 = e^{-9.64x^2}$  is chosen to span the range of resolvable wavenumbers with 10% amplitude at the Nyquist limit. The problem is solved using the DG correction function on Gauss–Legendre, equidistant and Gauss–Lobatto points as solution points. Figures 21 and 22 plot the evolution of the solution and the error norm respectively. Since the numerical wavespeeds for all three cases are identical, the difference in solutions is entirely attributed to the different distribution of energy among the numerical modes. As explained in Sect. 2.5, the choice of Gauss–Lobatto points for  $P = 2$  results in a spurious mode with dominant energy content at high wavenumbers. As this mode decays away, the numerical solution loses a sizable portion of its overall energy leading to the dissipated state in Fig. 21. The results in the case of equidistant and Gauss–Legendre points nearly overlap, which is to be expected as the energy content for a large portion of the spectrum is similar for these two choices. This example highlights the importance of the choice of solution points even for simple linear fluxes.

## 6 Conclusions

The contributions of this study can be divided into two categories. The first is concerned with a complete modal analysis of the FR formulation and the second with the identification of spectrally optimal FR schemes. We provide here a summary of the important conclusions.

Similar to the DG method, a  $P$ th order FR scheme results in  $P + 1$  numerical eigenmodes,  $P$  of which are spurious. For each of these modes, the dispersion and dissipation properties are obtained from the semi-discrete dispersion relation. The linear decomposition of the initial condition into the eigenvectors provides the relative energy distribution among the modes. With increase in polynomial order, the resolving efficiency increases primarily due to the reduction in dissipation at moderate wavenumbers. Additionally, the fraction of energy retained in the physical mode stays close to unity for a larger range of wavenumbers. The choice of correction function strongly affects the dispersion and dissipation properties, but

weakly affects the distribution of energy content between the modes. Finally, contrary to expectation, the choice of solution points is critical in that it strongly affects the distribution of energy among the modes. In particular, the choice of Gauss–Lobatto solution points can cause a cross-over point such that for a range of high wavenumbers, one of the spurious modes captures the dominant energy fraction. This energy gets lost due to the highly dissipative nature of spurious modes.

Spectrally optimal FR schemes are obtained by minimizing the error associated with wave propagation over the range of resolvable wavenumbers using a novel objective function that accounts for the multi-modal nature of the solution. The optimal member in the EFR family provides little advantage over the DG scheme. However, optimization over the entire range of available zeros of the correction function yields linearly stable FR schemes that provide considerably higher resolving efficiency than DG for  $P \geq 4$ . These schemes have the same formal order and achieve greater accuracy through optimal choices of the correction function. The resolving efficiency for these schemes is higher than standard implicit compact finite difference tridiagonal schemes as well. In particular, the 6th order OFR scheme provides similar resolution to the 8th order standard implicit compact difference scheme. CFL limits for the optimal schemes compare well with the DG scheme thereby ensuring that no extra effort is required in obtaining higher accuracy. Linear advection of wave-packets suggest that the advantage of using the proposed schemes applies to non-uniform grids as well. Due to the enhanced resolution, the greatest benefit is received for moderately high wavenumbers at about half the Nyquist limit.

The scope for future work includes the evaluation of spectrally optimal schemes on multi-dimensional elements. While it is intuitive to expect that the present schemes would continue to be optimal for quadrilaterals and hexahedra, using tensor products, an analytical proof or similar computational exercise should be carried out to ascertain this. The extension to simplex elements is more complicated. A characterization of the wave properties for triangles and tetrahedra would be an important step in understanding the wave properties of the FR formulation.

**Acknowledgments** The authors are grateful to Prof. S. K. Lele (Professor, Department of Aeronautics and Astronautics, Stanford University) for motivating the problem and advising in the choice of relevant test cases, and to Francisco Palacios (Engineering Research Associate, Department of Aeronautics and Astronautics, Stanford University) for his suggestions regarding the manuscript. The first author would also like to thank David Williams (CFD Engineer, Flight Sciences division, Boeing Commercial Airplanes) and Manuel López (Ph.D. candidate, Department of Aeronautics and Astronautics, Stanford University) for valuable suggestions regarding the optimization problem. The first author was supported in this effort by the Thomas V. Jones Stanford Graduate Fellowship.

## References

1. Tam, C.K.W.: Computational aeroacoustics: issues and methods. *AIAA J.* **33**(10), 1788–1796 (1995)
2. Visbal, M.R., Gaitonde, D.V.: Very high-order spatially implicit schemes for computational acoustics on curvilinear meshes. *J. Comp. Acous.* **09**, 1259 (2001)
3. Wang, M., Freund, J.B., Lele, S.K.: Computational prediction of flow-generated sound. *Annu. Rev. Fluid Mech.* **38**, 483512 (2006)
4. Moin, P., Mahesh, K.: Direct numerical simulation: a tool in turbulence research. *Annu. Rev. Fluid Mech.* **30**, 53978 (1998)
5. Hesthaven, J. S., Warburton, T.: *Nodal Discontinuous Galerkin Methods*. Springer Texts in Applied Mathematics, 54, (2008)
6. Lele, S.K.: Compact finite difference schemes with spectral-like resolution. *J. Comput. Phys.* **103**, 16–42 (1992)

7. Visbal, M.R., Gaitonde, D.V.: On the use of higher-order finite-difference schemes on curvilinear and deforming meshes. *J. Comput. Phys.* **181**, 155–185 (2002)
8. Chavent, G., Cockburn, B.: The local projection  $P^0 P^1$ -discontinuous-Galerkin finite element method for scalar conservation laws. *RAIRO Model. Math. Anal. Numer.* **23**, 565 (1989)
9. Lesaint, P., Raviart, P.A.: On a finite element method for solving the neutron transport equation. In: *Mathematical Aspects of Finite Elements in Partial Differential Equations*, p. 89. Academic Press, San Diego (1974)
10. Reed, W.H., Hill, T.R.: Triangular mesh methods for the neutron transport equation. Los Alamos Scientific Laboratory Report LA-UR-73-479 (1973)
11. Huynh, H.T.: A flux reconstruction approach to high-order schemes including discontinuous Galerkin methods. In: Huynh, H.T. (ed.) *AIAA Conference Paper*, 2007–4079 (2007)
12. Kopriva, D.A., Koliass, J.H.: A conservative staggered-grid Chebyshev multidomain method for compressible flows. *J. Comput. Phys.* **125**, 244–261 (1996)
13. Liu, Y., Vinokur, M., Wang, Z.J.: Spectral difference method for unstructured grids I: basic formulation. *J. Comput. Phys.* **216**, 780–801 (2006)
14. Vincent, P.E., Castonguay, P., Jameson, A.: A new class of high-order energy stable flux reconstruction schemes. *J. Sci. Comput.* **47**(1), 50–72 (2011)
15. Jameson, A., Vincent, P.E., Castonguay, P.: On the non-linear stability of flux reconstruction schemes. *J. Sci. Comput.* **50**(2), 434–445 (2012)
16. Castonguay, P., Vincent, P.E., Jameson, A.: A new class of high-order energy stable flux reconstruction schemes for triangular elements. *J. Sci. Comput.* **51**(1), 224–256 (2012)
17. Huynh, H.T.: High-order methods including discontinuous Galerkin by reconstructions on triangular meshes. In: *49th AIAA Aerospace Sciences Meeting AIAA 2011-44*
18. Williams, D.M., Jameson, A.: Energy stable flux reconstruction schemes for advection-diffusion problems on tetrahedra. *J. Sci. Comput.* (2013)
19. Castonguay, P., Williams, D.M., Vincent, P.E., Jameson, A.: Energy stable flux reconstruction schemes for advection-diffusion problems. *Comput. Methods Appl. Mech. Eng.* **267**, 400–417 (2013)
20. Whitham, G.B.: *Linear and Nonlinear Waves*. Pure and Applied Mathematics, vol. 42. Wiley, New York (2011)
21. Tam, C.K.W.: Dispersion relation preserving finite difference schemes for computational aeroacoustics. *J. Comput. Phys.* **107**, 262–281 (1993)
22. Adam, Y.: Highly accurate compact implicit methods and boundary conditions. *J. Comput. Phys.* **24**, 10–22 (1977)
23. Haras, Z., Ta'asan, S.: Finite difference schemes for long-time integration. *J. Comput. Phys.* **114**, 265–279 (1994)
24. Hirsch, R.S.: Higher order accurate difference solutions of fluid mechanics problems by a compact differencing technique. *J. Comput. Phys.* **19**, 90–109 (1975)
25. Sengupta, T.K., Ganeriwal, G., De, S.: Analysis of central and upwind compact schemes. *J. Comput. Phys.* **192**, 677–694 (2003)
26. Gottlieb, D., Orszag, S.A.: *Numerical Analysis of Spectral Methods*. SIAM, Philadelphia (1977)
27. Hu, F.Q., Hussaini, M.Y., Rasetarinera, P.: An analysis of the discontinuous Galerkin method for wave propagation problems. *J. Comput. Phys.* **151**, 921946 (1999)
28. Hu, F.Q., Atkins, H.L.: Eigensolution analysis of the discontinuous Galerkin method with nonuniform grids. *J. Comput. Phys.* **182**, 516–545 (2002)
29. Ainsworth, M.: Dispersive and dissipative behaviour of high order discontinuous Galerkin finite element methods. *J. Comput. Phys.* **198**, 106–130 (2004)
30. Vincent, P.E., Castonguay, P., Jameson, A.: Insights from von Neumann analysis of high-order flux reconstruction schemes. *J. Comput. Phys.* **230**, 81348154 (2011)
31. Van den Abeele, K.: *Development of High-order Accurate Schemes for Unstructured Grids*, Ph.D. thesis, Vrije Universiteit Brussel (2009)
32. Boyd, S., Vandenberghe, L.: *Convex Optimization*. Cambridge University Press, Cambridge (2004)
33. Powell, M.J.D.: A fast algorithm for nonlinearly constrained optimization calculations. In: *Numerical Analysis, Lecture Notes in Mathematics*, vol. 630, 144–157. Springer, Berlin (1978)
34. *Optimization Toolbox User's Guide—Version 5.0, (R2010a)*, The MathWorks Inc, Natick
35. Williams, D.M.: *Energy stable high-order methods for simulating unsteady, viscous, compressible flows on unstructured grids*. Thesis (Ph.D.)-Stanford University (2013)
36. Carpenter, M.H., Kennedy, C.: Fourth-order 2N-storage Runge–Kutta schemes, Technical Report TM 109112. NASA, NASA Langley Research Center (1994)
37. Kubatko E. J., Yeager B. A., Ketcheson, D. I.: Optimal strong-stability-preserving Runge-Kutta time discretizations for discontinuous galerkin methods. *J. Sci. Comput.* doi10.1007/s10915-013-9796-7